A machine learning-based stabilized finite element formulation for the mean stress computation in linear elasticity and coupled poroelasticity

Honório, Hermínio T.; Franceschini, Andrea; Ferronato, Massimiliano; Hajibeygi, Hadi

DOI
10.1016/j.cma.2025.118515

Publication date
2025

Document Version
Final published version

Published in
Computer Methods in Applied Mechanics and Engineering

Citation (APA)
Honório, H. T., Franceschini, A., Ferronato, M., & Hajibeygi, H. (2025). A machine learning-based stabilized finite element formulation for the mean stress computation in linear elasticity and coupled poroelasticity. *Computer Methods in Applied Mechanics and Engineering*, *449*, Article 118515. https://doi.org/10.1016/j.cma.2025.118515

Computer Methods in Applied Mechanics and Engineering 449 (2026) 118515

Contents lists available at ScienceDirect

Comput. Methods Appl. Mech. Engrg.

journal homepage: www.elsevier.com/locate/cma

A machine learning-based stabilized finite element formulation for the mean stress computation in linear elasticity and coupled poroelasticity

Hermínio T. Honório [a,*], Andrea Franceschini [b], Massimiliano Ferronato [b], Hadi Hajibeygi [a]

[a] Faculty of Civil Engineering and Geosciences, Delft University of Technology, Stevinweg 1, 2628CN, Delft, the Netherlands
[b] Dept. of Civil, Environmental and Architectural Engineering, University of Padova, Padova, Italy

ARTICLE INFO

Keywords:
Poroelasticity
Finite elements
Stabilization
Physical influence scheme
Machine learning

ABSTRACT

This work addresses numerical instabilities that can appear when computing the mean stress in linear elasticity and coupled poroelasticity problems discretized with low-order finite elements. The linear elasticity and coupled poroelasticity models are solved using both primal and mixed finite element formulations. Stabilization is obtained by enriching the finite element approximation with an approximation of the Laplacian of displacements. This Laplacian is then evaluated with the Physical Influence Scheme (PIS) by leveraging the underlying governing equation. A key step in the proposed stabilization is the calculation of a parameter h, often computed in the literature as a characteristic length of the element. In this work, we calculate h by solving an optimization problem at the element level. To avoid the high computational cost associated with this procedure, a machine learning model is proposed to predict the optimal h. The benefit of combining PIS with an appropriate computation of h is that the resulting stabilization scheme does not rely on any type of heuristic or user-specified tuning parameter, as often required in other stabilization methods. The results show that the proposed stabilization strategy can effectively remove both saddle-point and Gibbs mean stress oscillations in linear elasticity. We also report, for the first time, that mean stress oscillations can also appear when solving coupled poroelasticity problems, and, differently from pore pressure oscillations (which naturally vanish with time), mean stress instabilities are persistent throughout the whole simulation time, unless deliberately removed. The proposed stabilized mixed formulation is able to remove both pore pressure and mean stress oscillations in coupled poroelasticity problems. Finally, the calculation of h is shown to be critical for the quality of the stabilization, with the machine learning-based approach providing the best compromise between numerical diffusion and accuracy.

1. Introduction

The presence of numerical oscillations is a common issue in the finite element (FE) solution of many physical problems. In addition to compromising accuracy, these spatial oscillations have no physical meaning and can seriously compromise the reliability of the results. This issue is tightly linked to the mathematical structure of the governing equations, the selection of the discretization spaces

* Corresponding author.
E-mail address: H.TasinafoHonorio@tudelft.nl (H.T. Honório).

https://doi.org/10.1016/j.cma.2025.118515
Received 31 July 2025; Received in revised form 19 October 2025; Accepted 20 October 2025
Available online 5 November 2025

for their numerical solution and the material properties of the physical problem. For instance, when continuous functions are used to approximate the solution, e.g. classical piecewise polynomials used in FE discretizations, oscillations may appear in regions where the solution is discontinuous (or a very sharp gradient is present)—this is often referred to as Gibbs phenomenon [1,2]. Alternatively, strong numerical oscillations can appear in problems mathematically assuming a saddle-point structure, such as those approaching incompressibility limits, in linear elasticity, coupled undrained consolidation, incompressible flows, among others. The saddle-point problem originated from the incompressibility constraint is well-known to cause spurious oscillations when the interpolation pairs do not satisfy the so-called Ladyzhenskaya-Babuška-Brezzi (LBB or *inf-sup*) condition [3–6]. Regardless of the origin and the problem at hand, spurious oscillations must be avoided in order to ensure physically consistent numerical results. In this paper, numerical instabilities affecting the pore pressure and mean stress solutions are investigated in the context of linear elasticity and coupled poroelasticity problems.

Mean stress oscillations have been extensively studied in solid mechanics, especially for nearly incompressible materials. In this case, a common approach is to modify the classical equations of linear elasticity to separate the mean stress from the stress tensor, and include a pressure-like equation to prescribe the volumetric constraint [7,8]. This mixed displacement/mean stress ($\mathbf{u} - \sigma_v$) formulation becomes mathematically equivalent to the Stokes model [9], which is known to be unstable for interpolation pairs not satisfying the LBB condition (e.g., equal-order interpolation pairs). Due to this similarity, stabilization techniques can be adapted from one model to the other. One example is the application of the Galerkin Least Square (GLS), originally developed for Stokes' equations [10], to solid mechanics [11–13]. Another important contribution is the variational multiscale (VMS) method, based on the idea of splitting the solution into coarse and fine scales [14,15], and successfully applied to (nearly-)incompressible solids [16–22]. Similarly to VMS, other methods also attempt to capture sub-grid effects, such as the finite increment calculus (FIC) [23,24] and residual free bubbles [25–28]. Also worth mentioning are the B-bar [29] and F-bar [30] methods, which provide stable solutions while preserving the displacement-based structure of the problem [31]. These works give a general idea of stabilization methods devised for incompressible solid mechanics, even though not exhaustive.

In coupled poroelasticity problems, governed by Biot's consolidation theory [32], the linear momentum balance equation is coupled with the fluid mass balance equation in deformable porous media. In this case, the primary unknowns are usually the displacement ($\mathbf{u}$) and pore pressure (p), so the problem resembles the mixed $\mathbf{u} - \sigma_v$ formulation for incompressible solids discussed above. Furthermore, a combination of reduced hydraulic properties and small time step size [33,34] can lead the model to approach a saddle-point problem during the initial simulation times, thus causing spurious pore pressure oscillations to appear when the discretization spaces are not LBB-stable. Naturally, many of the stabilization techniques already developed for other saddle-point problems, such as Stokes flow and incompressible solids, have been also proposed for coupled poroelasticity. For instance, GLS has been extended to coupled poroelasticity [35,36]; the Polynomial-Pressure-Projection, originally developed for Stokes flow [37], was also applied to coupled poromechanics [38]; in Preisig and Prévost [39], FIC [23] was extended to coupled poromechanics and compared with other stabilization schemes, such as the fluid pressure Laplacian (FPL) [40] and PPP [38]. More recently, the Physical Influence Scheme[1] (PIS), originally devised for incompressible Navier-Stokes model [41–45], was used to mitigate pressure oscillations originating from a finite volume (FV) formulation of coupled poroelasticity problems [46]; FPL and PPP were also employed to stabilize a mixed continuous-enriched Galerkin (CG/EG) formulation [47]; other works employ a macro-element jump-jump stabilization for mixed and mixed hybrid low-order discretizations of coupled poromechanics [48–50].

As discussed above, spurious pore pressure oscillations have been extensively investigated by many authors. However, to the best of the authors' knowledge, the present work reports for the first time a method to address the issue of spurious mean stress oscillations in the numerical solution of coupled poroelasticity problems. Since the solution vector usually provides only displacements and pore pressure fields—which are oscillation-free, as long as a stable formulation is employed—such spurious mean stress oscillations are likely to go unnoticed, unless the mean stress field is explicitly plotted. These oscillations can represent a serious issue for mean stress-dependent constitutive models, such as the well-known Modified Cam-Clay (MCC). One of the novelties of the present work is to propose a stabilization scheme that addresses both pore pressure and mean stress oscillations in coupled poroelasticity problems. A three-field mixed FE formulation is proposed, with piecewise linear interpolations for $\mathbf{u}$, σ_v, and p fields. The $\mathbf{u} - \sigma_v - p$ mixed formulation is obtained by splitting the stress tensor into its deviatoric and spherical parts, as commonly done for incompressible elasticity. A similar approach has been adopted for coupled poroelasticity in Lee et al. [51], but the authors used piecewise-constant mean stress interpolations, and no stabilization was used, since the focus was on robust preconditioning.

The stabilization strategy adopted in this work consists of enriching the displacement field approximation, mimicking a higher-order finite element. This is achieved by expanding the approximation using Taylor series and including a higher-order term, namely the Laplacian of displacements. Next, we adopt PIS to evaluate this Laplacian based on the momentum equation, as proposed in Honório et al. [46]. As compared to Honório et al. [46], the present work extends the technique in three aspects. Firstly, PIS was originally developed for a FV formulation, but is adapted here to the FE method. Secondly, PIS is applied for the first time to stabilized mean stress oscillations in linear elasticity problems using a two-field mixed FE formulation. Thirdly, PIS is combined to a three-field mixed FE formulation to achieve stabilization for both mean stress and pore pressure fields in coupled poroelasticity problems. As in many schemes (e.g., GLS, PPP, FLP, FIC, etc), the stabilization terms added to the system depend on a parameter h, which has been often interpreted as characteristic length of the element for the sake of its computation. Different choices include the maximum edge length of the element, the radius of an inscribed sphere, etc. In the proposed stabilization scheme, the value

[1] This method was originally presented under the name of Finite Element Differencing Scheme (FIELDS) in Schneider and Raw [41], and eventually renamed as Physical Influence Scheme (PIS), as in Darbandi et al. [42], for instance.

of h is regarded as a parameter which is introduced to maximize the accuracy of the displacement finite element approximation. Based on this interpretation, we propose to calculate the value of h by solving an optimization problem for each element in order to provide optimal approximations for the displacement field. Unfortunately, this procedure is rather expensive, which motivated the development of a machine learning model to predict the optimal values of h for all grid elements at an affordable cost. The combination of this improved h parameter calculation with the physics-based Laplacian approximation, provided by PIS, results in a stabilization scheme that does not rely on heuristic or user-specified tuning parameters, as common in other stabilization methods, such as the PPP and VMS.

This paper is organized as follows. Section 2 presents both the linear elasticity model for nearly incompressible solids and the coupled poroelasticity model. The primal weak formulations for linear elasticity ($\mathbf{u}$) and for coupled poroelasticity ($\mathbf{u} - p$) are presented in Section 3. In the sequence, Section 4 presents the mixed weak formulations for the same two models. The finite element approximations for both primal and mixed formulations are introduced in Section 5. In Section 6, the stabilization strategy is discussed in details, connecting the Taylor series expansions to the use of PIS. The optimization strategy and the machine-learning model used to calculate the optimal values of h are introduced in Section 7. Finally, the numerical experiments and test cases are presented in Section 9, and Section 10 closes the presentation with our conclusions.

2. Mathematical models

In this work, we investigate the solution of the linear elasticity and the coupled poroelasticity models. Here, we present the equations that are common to both models, with the particularities of each model described in the following subsections.

Both models depend on the linear momentum balance equation, which can be written as

$$-\nabla \cdot \boldsymbol{\sigma} = \mathbf{b}, \tag{1}$$

where $\boldsymbol{\sigma}$ is the rank-2 stress tensor and $\mathbf{b}$ is the vector of body forces. For simplicity, and with no loss of generality, all body forces and gravitational effects are neglected from this work.

By considering small strains, the compatibility equation reads

$$\boldsymbol{\epsilon}(\mathbf{u}) = \frac{1}{2}\left(\nabla \mathbf{u} + \nabla \mathbf{u}^T\right), \tag{2}$$

where $\mathbf{u}$ denotes the displacement vector. Finally, the volumetric strain and mean stress are respectively defined as

$$\varepsilon_v = \nabla \cdot \mathbf{u} \quad \text{and} \quad \sigma_v = K\varepsilon_v, \tag{3}$$

with K representing the bulk modulus.

2.1. Linear elasticity

Considering Hooke's law, the constitutive equation for linear elasticity and isotropic material reads

$$\boldsymbol{\sigma} = 2G\boldsymbol{\epsilon} + \lambda\varepsilon_v \mathbf{I}, \tag{4}$$

with G and λ denoting the shear modulus and Lamé's first parameter, respectively, and $\mathbf{I}$ is the rank-2 identity tensor. The linear elasticity model is, therefore, formed by combining Eqs. (1), (2), (3) and (4) subjected to appropriate boundary conditions.

2.2. Coupled poroelasticity

For coupled poroelasticity problems, where Terzaghi's effective stress principle applies, the total stress tensor can be expressed as

$$\boldsymbol{\sigma} = 2G\boldsymbol{\epsilon} + \left(\lambda\varepsilon_v - \alpha p\right)\mathbf{I}, \tag{5}$$

where p represents the pore pressure, and Biot's coefficient is given by $\alpha = 1 - c_s K$, with c_s denoting the solid grain compressibility.

The second governing equation consists of the mass conservation equation for the fluid phase in deformable porous media. Considering Darcy's law and neglecting buoyancy effects, it reads

$$\frac{1}{Q}\dot{p} - \nabla \cdot \left(\frac{\mathbf{k}}{\mu} \cdot \nabla p\right) + \alpha\dot{\varepsilon}_v = f, \tag{6}$$

where f is the fluid source term, and $\mathbf{k}$ and μ denote absolute permeability tensor and fluid viscosity, respectively. Moreover, Biot's modulus is given by $Q = \left[\phi c_f + (\alpha - \phi)c_s\right]^{-1}$, with c_f and ϕ respectively denoting fluid compressibility and porosity.

For coupled poroelasticity, the problem consists of finding $\mathbf{u}$ and p fields that satisfy Eqs. (1), (2), (3), (5), and (6) subjected to appropriate initial and boundary conditions.

3. Primal weak formulations

In this work, approximations for displacement and pressure fields are obtained using first-order Sobolev spaces (H^1). Consider a domain Ω bounded by Γ, such that $\Gamma = \Gamma^u_d \cup \Gamma^u_n = \Gamma^p_d \cup \Gamma^p_n$, with $\Gamma^u_d \cap \Gamma^u_n = \Gamma^p_d \cap \Gamma^p_n = \emptyset$, where Γ^u_d and Γ^p_d are the surfaces on which Dirichlet boundary conditions $\bar{\mathbf{u}}$ and $\bar{p}$ are applied to $\mathbf{u}$ and p, respectively, while Γ^u_n and Γ^p_n are the corresponding surfaces for Neumann conditions. In this manner, we define continuous trial function spaces as

$$\mathcal{U} = \{\mathbf{u} : \Omega \to \mathbb{R}^3 \mid \mathbf{u} \in \mathbf{H}^1, \mathbf{u} = \bar{\mathbf{u}} \text{ on } \Gamma^u_d\},$$
$$\mathcal{P} = \{p : \Omega \to \mathbb{R} \mid p \in H^1, p = \bar{p} \text{ on } \Gamma^p_d\},$$

and the corresponding continuous test (weighting) function spaces as

$$\mathcal{U}_0 = \{\mathbf{w} : \Omega \to \mathbb{R}^3 \mid \mathbf{w} \in \mathbf{H}^1, \mathbf{w} = \mathbf{0} \text{ on } \Gamma^u_d\},$$
$$\mathcal{P}_0 = \{q : \Omega \to \mathbb{R} \mid q \in H^1, q = 0 \text{ on } \Gamma^p_d\}.$$

3.1. Linear elasticity

According to Eqs. (4), (2) and (3), we can represent the stress tensor for linear elasticity as a function of displacement, that is, $\boldsymbol{\sigma} = \boldsymbol{\sigma}(\mathbf{u})$. In this manner, the weak form of the momentum balance equation can be written as

$$\int_\Omega \boldsymbol{\varepsilon}(\mathbf{w}) : \boldsymbol{\sigma}(\mathbf{u}) \mathrm{d}\Omega - \int_{\Gamma^u_n} \mathbf{w} \cdot \mathbf{t} \mathrm{d}\Gamma = \int_\Omega \mathbf{w} \cdot \mathbf{b} \mathrm{d}\Omega \qquad \forall\ \mathbf{w} \in \mathcal{U}_0, \tag{7}$$

where $\mathbf{t}$ is the traction vector imposed on Γ^u_n.

3.2. Coupled poroelasticity

For the case of coupled poroelasticity, the stress tensor is also a function of pore pressure (see Eq. 5), therefore, the weak form of the momentum and mass balance equations read

$$\int_\Omega \boldsymbol{\varepsilon}(\mathbf{w}) : \boldsymbol{\sigma}(\mathbf{u}) \mathrm{d}\Omega - \int_{\Gamma^u_n} \mathbf{w} \cdot \mathbf{t} \mathrm{d}\Gamma = \int_\Omega \mathbf{w} \cdot \mathbf{b} \mathrm{d}\Omega \qquad \forall\ \mathbf{w} \in \mathcal{U}_0, \tag{8}$$

$$\int_\Omega q \left(\frac{1}{Q} \dot{p} + \alpha \dot{\varepsilon}_v \right) \mathrm{d}\Omega + \int_\Omega \frac{\mathbf{k}}{\mu} \cdot \nabla p \cdot \nabla q \mathrm{d}\Omega - \int_{\Gamma^p_n} v_n q \mathrm{d}\Gamma = \int_\Omega q f \mathrm{d}\Omega \qquad \forall\ q \in \mathcal{P}_0, \tag{9}$$

where v_n is the prescribed fluid phase velocity normal to boundary Γ^p_n.

4. Mixed weak formulations

The trial function space for approximating the mean stress field is defined as

$$\mathcal{S} = \{\sigma_v : \Omega \to \mathbb{R} \mid \sigma_v \in H^1, \sigma_v = \bar{\sigma}_v \text{ on } \Gamma^\sigma_d\}, \tag{10}$$

where the values $\bar{\sigma}_v$ prescribed on the portion Γ^σ_d of the boundary Γ is consistent with conditions set on the displacement field. The corresponding test function space reads

$$\mathcal{S}_0 = \{v : \Omega \to \mathbb{R} \mid v \in H^1, v = 0 \text{ on } \Gamma^\sigma_d\}. \tag{11}$$

4.1. Linear elasticity

The foundation for the mixed formulation is the decomposition of the stress tensor into a deviatoric part, $\tilde{\boldsymbol{\sigma}}$, and a spherical part, that is

$$\boldsymbol{\sigma} = \tilde{\boldsymbol{\sigma}} + \sigma_v \mathbf{I},$$

where the deviatoric stress relates to the deviatoric strain $\tilde{\boldsymbol{\varepsilon}}$ by

$$\tilde{\boldsymbol{\sigma}} = 2G\tilde{\boldsymbol{\varepsilon}},$$

in which

$$\boldsymbol{\varepsilon} = \tilde{\boldsymbol{\varepsilon}} + \frac{1}{3}\varepsilon_v \mathbf{I} \quad \rightarrow \quad \tilde{\boldsymbol{\varepsilon}} = \boldsymbol{\varepsilon} - \frac{1}{3}\varepsilon_v \mathbf{I}.$$

Additionally, since $\sigma_v = K\varepsilon_v$, it follows that the stress tensor can be written as a function of displacement and mean stress, that is,

$$\boldsymbol{\sigma}(\mathbf{u}, \sigma_v) = 2G\left(\boldsymbol{\varepsilon} - \frac{1}{3}\varepsilon_v \mathbf{I}\right) + \sigma_v \mathbf{I} \tag{12}$$

In this manner, the governing equations consist of the linear momentum balance equation expressed as,

$$-\nabla \cdot \boldsymbol{\sigma}(\mathbf{u}, \sigma_v) = \mathbf{b}, \tag{13}$$

and the relationship between mean stress and volumetric strain, which describes mass balance for the solid phase, i.e.,

$$\sigma_v - K\nabla \cdot \mathbf{u} = 0. \tag{14}$$

The weak forms of Eqs. (13) and (14) read

$$\int_\Omega \boldsymbol{\varepsilon}(\mathbf{w}) : \boldsymbol{\sigma}(\mathbf{u}, \sigma_v)\mathrm{d}\Omega - \int_{\Gamma_n^u} \mathbf{w} \cdot \mathbf{t}\mathrm{d}\Gamma = \int_\Omega \mathbf{w} \cdot \mathbf{b}\mathrm{d}\Omega \qquad \forall\ \mathbf{w} \in \mathcal{U}_0, \tag{15}$$

$$\int_\Omega v\big(\sigma_v - K\nabla \cdot \mathbf{u}\big)\mathrm{d}\Omega = 0 \qquad \forall\ v \in \mathcal{S}_0. \tag{16}$$

4.2. Coupled poroelasticity

Following the stress decomposition presented in the previous subsection, the total stress tensor for poroelasticity is obtained by simply adding the pore pressure to Eq. (12). In this manner, the stress tensor becomes a function of displacement, mean stress and pore pressure, i.e.,

$$\boldsymbol{\sigma}(\mathbf{u}, \sigma_v, p) = 2G\Big(\boldsymbol{\varepsilon} - \frac{1}{3}\varepsilon_v \mathbf{I}\Big) + \big(\sigma_v - \alpha p\big)\mathbf{I}. \tag{17}$$

The momentum balance equation assumes the form

$$-\nabla \cdot \boldsymbol{\sigma}(\mathbf{u}, \sigma_v, p) = \mathbf{b}. \tag{18}$$

As a result, the mixed formulation for coupled poroelasticity is obtained from the weak form of Eqs. (18), (14), and (6), which results in

$$\int_\Omega \boldsymbol{\varepsilon}(\mathbf{w}) : \boldsymbol{\sigma}(\mathbf{u}, \sigma_v, p)\mathrm{d}\Omega - \int_{\Gamma_n^u} \mathbf{w} \cdot \mathbf{t}\mathrm{d}\Gamma = \int_\Omega \mathbf{w} \cdot \mathbf{b}\mathrm{d}\Omega, \qquad \forall\ \mathbf{w} \in \mathcal{U}_0, \tag{19}$$

$$\int_\Omega v\big(\sigma_v - K\nabla \cdot \mathbf{u}\big)\mathrm{d}\Omega = 0, \qquad \forall\ v \in \mathcal{S}_0, \tag{20}$$

$$\int_\Omega q\left(\frac{1}{Q}\dot{p} + \alpha\dot{\varepsilon}_v\right)\mathrm{d}\Omega + \int_\Omega \frac{\mathbf{k}}{\mu} \cdot \nabla p \cdot \nabla q\mathrm{d}\Omega - \int_{\Gamma_n^p} v_n q\mathrm{d}\Gamma = \int_\Omega f q\mathrm{d}\Omega, \qquad \forall\ q \in \mathcal{P}_0. \tag{21}$$

5. Finite element discretization

The solutions to the weak forms defined in the previous sections are numerically approximated by finite elements. As usual, the domain is divided into discrete elements τ^h, with the solutions $(\mathbf{u}^h, \sigma_v^h, p^h)$ and the test functions $(\mathbf{w}^h, v^h, q^h)$ belonging to the following finite element spaces,

$$\mathbf{u}^h \in \mathcal{U}^h \subset \mathcal{U}, \quad \mathbf{w}^h \in \mathcal{U}_0^h \subset \mathcal{U}_0, \tag{22}$$

$$\sigma_v^h \in \mathcal{S}^h \subset \mathcal{S}, \quad v^h \in \mathcal{S}_0^h \subset \mathcal{S}_0, \tag{23}$$

$$p^h \in \mathcal{P}^h \subset \mathcal{P}, \quad q^h \in \mathcal{P}_0^h \subset \mathcal{P}_0. \tag{24}$$

The finite element spaces are constructed with Continuous Galerkin approximations using piecewise linear basis functions. Moreover, the integration scheme is performed using the lowest-order quadrature rule, that is, a single integration point located at the centroid of each tetrahedral element.

The exact solutions are approximated as

$$\mathbf{u} \approx \mathbf{u}^h = \mathbf{u}^h(\mathbf{x}, t) = \mathbf{N}_u(\mathbf{x})\hat{\mathbf{u}}(t) \tag{25}$$

$$\sigma_v \approx \sigma_v^h = \sigma_v^h(\mathbf{x}, t) = \mathbf{N}(\mathbf{x})\hat{\sigma}_v(t) \tag{26}$$

$$p \approx p^h = p^h(\mathbf{x}, t) = \mathbf{N}(\mathbf{x})\hat{p}(t) \tag{27}$$

where $\hat{\mathbf{u}}(t)$, $\hat{\sigma}_v(t)$ and $\hat{p}(t)$ are the vectors of unknowns at the grid nodes, $\mathbf{N}(\mathbf{x})$ represent the element shape functions, and $\mathbf{N}_u(\mathbf{x})$ is a matrix rearrangement of the same shape functions to properly multiply the corresponding displacement components of $\mathbf{u}$. The corresponding gradients are approximated as

$$\boldsymbol{\varepsilon}(\mathbf{u}^h) = \mathbf{B}\hat{\mathbf{u}}, \quad \nabla p^h = \mathbf{G}\hat{p}, \quad \text{and} \quad \nabla\sigma_v^h = \mathbf{G}\hat{\sigma}_v,$$

with $\mathbf{G}$ denoting an array of shape function derivatives that recovers the gradient field of a scalar (p^h and σ_v^h). Similarly, $\mathbf{B}$ is also an array of shape function derivatives that recovers the symmetric gradient of $\mathbf{u}$.

Next, we define the following matrices

$$\mathrm{K}_1 = \int_\Omega \mathbf{B}^T \mathbb{C}\mathbf{B}\mathrm{d}\Omega, \qquad \mathrm{K}_2 = \int_\Omega 2G\mathbf{B}^T\mathbf{B}\mathrm{d}\Omega, \qquad \mathrm{F} = \int_\Omega \frac{1}{\mu}\mathbf{G}^T\mathbf{k}\mathbf{G}\mathrm{d}\Omega,$$

$$\mathrm{A}_1 = \int_\Omega \frac{1}{K}\mathbf{N}^T\mathbf{N}\mathrm{d}\Omega, \qquad \mathrm{A}_2 = \int_\Omega \frac{1}{Q}\mathbf{N}^T\mathbf{N}\mathrm{d}\Omega, \qquad \mathbf{f}_u = \int_{\Gamma_n^u} \mathbf{w}^h \cdot \mathbf{t}\mathrm{d}\Gamma + \int_\Omega \mathbf{w}^h \cdot \mathbf{b}\mathrm{d}\Omega, \tag{28}$$
$$\mathrm{B}_1 = \int_\Omega \mathbf{N}^T\mathbf{i}\mathbf{B}\mathrm{d}\Omega, \qquad \mathrm{B}_2 = -\int_\Omega \alpha\mathbf{N}^T\mathbf{i}\mathbf{B}\mathrm{d}\Omega, \qquad \mathbf{f}_p = \int_{\Gamma_n^p} v_n q^h \mathrm{d}\Gamma + \int_\Omega f q^h \mathrm{d}\Omega$$

where $\mathbb{C}$ is the elastic stiffness matrix (Voigt notation) and $\mathbf{i}$ is the Kronecker delta in vector form. These matrices will be used to compose the linear systems resulting from the FE discretization in the following subsections.

5.1. Linear elasticity

Considering the finite element approximations shown in this section and the matrices defined in Eq. (28), the discretized primal and mixed formulations can be obtained. These formulations assume the forms presented below.

Primal formulation:

$$\left[\mathrm{K}_1\right]\left[\hat{\mathbf{u}}\right] = \left[\mathbf{f}_u\right].$$

Mixed formulation:

$$\begin{bmatrix} \mathrm{K}_2 & \mathrm{B}_1 \\ \mathrm{B}_1^T & -\mathrm{A}_1 \end{bmatrix} \begin{bmatrix} \hat{\mathbf{u}} \\ \hat{\sigma}_v \end{bmatrix} = \begin{bmatrix} \mathbf{f}_u \\ 0 \end{bmatrix}.$$

5.2. Coupled poroelasticity

The mass conservation equation for the fluid phase also involves the time derivatives of p and ϵ_v. Therefore, a time integration is also performed between times n and $n+1$ by using a backward Euler scheme. The resulting linear systems for both primal and mixed formulations are presented below.

Primal formulation:

$$\begin{bmatrix} \mathrm{K}_1 & \mathrm{B}_2 \\ \mathrm{B}_2^T & -\left(\mathrm{A}_2 + \Delta t\mathrm{F}\right) \end{bmatrix} \begin{bmatrix} \hat{\mathbf{u}} \\ \hat{p} \end{bmatrix}^{n+1} = \begin{bmatrix} \mathbf{f}_u \\ \mathbf{f}_p \end{bmatrix} + \begin{bmatrix} 0 & 0 \\ \mathrm{B}_2^T & -\mathrm{A}_2 \end{bmatrix} \begin{bmatrix} \hat{\mathbf{u}} \\ \hat{p} \end{bmatrix}^n.$$

Mixed formulation:

$$\begin{bmatrix} \mathrm{K}_2 & \mathrm{B}_1 & \mathrm{B}_2 \\ \mathrm{B}_1^T & -\mathrm{A}_1 & 0 \\ \mathrm{B}_2^T & 0 & -\left(\mathrm{A}_2 + \Delta t\mathrm{F}\right) \end{bmatrix} \begin{bmatrix} \hat{\mathbf{u}} \\ \hat{\sigma}_v \\ \hat{p} \end{bmatrix}^{n+1} = \begin{bmatrix} \mathbf{f}_u \\ 0 \\ \mathbf{f}_p \end{bmatrix} + \begin{bmatrix} 0 & 0 & 0 \\ 0 & 0 & 0 \\ \mathrm{B}_2^T & 0 & -\mathrm{A}_2 \end{bmatrix} \begin{bmatrix} \hat{\mathbf{u}} \\ \hat{\sigma}_v \\ \hat{p} \end{bmatrix}^n.$$

6. Stabilization scheme

As previously introduced in Sections 3 and 4, the present work adopts the same piecewise linear interpolation functions for displacement, pressure, and mean stress fields. As it is well-known, this combination of spaces is not LBB-stable and require some stabilization. We obtain this improved approximation by using Taylor series expansion to add a higher order term (Laplacian of $\mathbf{u}$) to the interpolation function for the displacement field. Then we use PIS to evaluate this higher order term in a convenient physics-based approach. When substituted into the governing equations, this improved interpolation function for the displacement field originates additional terms in the weak form that can stabilize the solution by introducing numerical diffusion.

To build our stabilization term, let us first discuss how to approximate a generic scalar function $\psi = \psi(\mathbf{x})$ at the centroid of an element of cubic shape with size L. Next, we discuss how the resulting expression can be generalized to a tetrahedral element, which is our goal in this work. In fact, we propose to approximate the function at the element centroid precisely because it coincides with the integration (Gauss) point of a linear tetrahedral element.

In Appendix A, it is shown that if the values of a function ψ are given at the vertices of a cube, and the Laplacian of ψ is known at the centroid, then the value of ψ can be approximated at the element centroid by the following expression:

$$\psi(\mathbf{x}_c) \approx \frac{1}{8}\sum_{i=1}^{8}\psi(\mathbf{x}_i) - \frac{L^2}{8}\nabla^2\psi(\mathbf{x}_c), \tag{29}$$

where $\mathbf{x}_i$ denotes the coordinates of the element vertices. Notice that the first term at the right-hand side of Eq. (29) is:

$$\frac{1}{8}\sum_{i=1}^{8}\psi(\mathbf{x}_i) = \mathbf{N}(\mathbf{x}_c)\hat{\psi} = \psi^h(\mathbf{x}_c). \tag{30}$$

Combining Eqs. (30) and (29), a general expression for approximating $\psi(\mathbf{x}_c)$ at the centroid of the cube can be expressed as

$$\psi(\mathbf{x}_c) \approx \psi^h(\mathbf{x}_c) - h^2\nabla^2\psi(\mathbf{x}_c). \tag{31}$$

where h is a scaling parameter of the Laplacian term. For polynomial functions up to degree 3 and for a cube of size L, as in Fig. A.18, Eq. (31) provides the exact value of $\psi(\mathbf{x}_c)$ as long as $h^2 = L^2/8$. For higher-order polynomial functions, or non-polynomial functions,

$h^2 = L^2/8$ still provides an accurate approximation of $\psi(\mathbf{x}_c)$, although it is no more exact. In case the element is not a cube, then the value of h for which Eq. (31) is exact cannot be found, but it is still possible to find h that provides the most accurate approximation of $\psi(\mathbf{x}_c)$.

Eq. (31) can be extended to a vector valued function, and an improved expression to approximate the displacement vector field reads

$$\mathbf{u} \approx \mathbf{u}^h - h^2 \nabla^2 \mathbf{u}, \tag{32}$$

where $\mathbf{u}$ is the exact solution and $\mathbf{u}^h$ is the classical finite element approximation (i.e., Eq. 25). The calculation of parameter h will be addressed in Section 7. In the next subsection, we discuss how to approximate the Laplacian of displacement in Eq. (32).

6.1. The physical influence scheme (PIS)

When deriving Eq. (32), it was assumed the exact Laplacian of $\mathbf{u}$ is given at the integration point. However, in practice this is not the case, and $\nabla^2\mathbf{u}$ must be approximated as well. For this purpose, PIS allows for the computation of this higher-order term based on the physics of the problem. Other Laplacian reconstruction methods (see Jansen et al. [52], for instance) could be employed in Eq. (32) and this might be an interesting development for future extension of this work.

Let us consider the linear momentum balance equation evaluated on a single grid element, where the material properties are constant, and use the stress decomposition equation (Eq. 17). In this way, the momentum balance equation can be written as

$$G\nabla^2\mathbf{u} + \frac{G}{3}\nabla\varepsilon_v + \nabla\sigma_v - \alpha\nabla p \approx 0. \tag{33}$$

Substituting $\varepsilon_v = \sigma_v/K$ and solving for the Laplacian leads to

$$\nabla^2\mathbf{u} \approx \frac{\alpha}{G}\nabla p - \left(\frac{1}{3K} + \frac{1}{G}\right)\nabla\sigma_v. \tag{34}$$

Eq. (34) reveals that the Laplacian of displacement is proportional to the gradients of pressure and mean stress. Furthermore, the constants of proportionality are originated from the underlying governing equation, therefore, the balance between $\nabla^2\mathbf{u}$, ∇p, and $\nabla\sigma_v$ is physically consistent. Calculating these two gradients is now perfectly possible with the linear shape functions. For this purpose, we introduce the finite element approximations for p and σ_v, defined in Eqs. (27) and (26), respectively, yielding

$$\nabla^2\mathbf{u} \approx \frac{\alpha}{G}\nabla p^h - \left(\frac{1}{3K} + \frac{1}{G}\right)\nabla\sigma_v^h. \tag{35}$$

From our experience, keeping the term $\frac{1}{3K}\nabla\sigma_v^h$ in Eq. (35) is beneficial in some situations, but not in others. For the primal formulation of the coupled poroelastic model, the whole term involving $\nabla\sigma_v^h$ must be neglected from Eq. (35), since σ_v is not explicitly solved. Additionally, we are also interested in investigating the impact of the term ∇p^h in the stabilization scheme. In order to cover all these possibilities, we rewrite Eq. (35) as

$$\nabla^2\mathbf{u} \approx a_1\frac{\alpha}{G}\nabla p^h - \left(\frac{a_2}{3K} + \frac{a_3}{G}\right)\nabla\sigma_v^h, \tag{36}$$

where a_1, a_2 and a_3 are chosen to be either 0 or 1. It is also interesting to notice that the term in parenthesis in Eq. (36) equals to $3/E$ when $a_2 = a_3 = 1$, where E is the Young's modulus.

Finally, by substituting Eq. (36) into Eq. (32), we obtain the following approximation for the displacement field

$$\mathbf{u} \approx \mathbf{u}^h - a_1 h^2 \frac{\alpha}{G}\nabla p^h + h^2\left(\frac{a_2}{3K} + \frac{a_3}{G}\right)\nabla\sigma_v^h. \tag{37}$$

For the linear elasticity model, Eq. (37) is used to approximate the displacement field in the mean stress equation, that is, Eq. (16). For the coupled poroelasticity model, the stabilization can be introduced into Eqs. (20) and/or (21).

6.2. Stabilized mixed elasticity

In this case, we disregard the pressure gradient from the stabilized approximation of $\mathbf{u}$ by choosing $a_1 = 0$ in Eq. (37) and substitute it into Eq. (16), i.e.,

$$\int_\Omega v^h\left\{\frac{1}{K}\sigma_v^h - \nabla\cdot\mathbf{u}^h - \nabla\cdot\left[h^2\left(\frac{a_2}{3K} + \frac{a_3}{G}\right)\nabla\sigma_v^h\right]\right\}\mathrm{d}\Omega = 0, \qquad \forall\ v^h \in \mathcal{S}_0^h.$$

We use integration by parts to evaluate the rightmost term inside the integral. Notice that the boundary term does not appear because the stabilization corresponds to a pure homogeneous Neumann Laplace problem. After this procedure, the following equation is obtained

$$\int_\Omega v^h\left(\frac{1}{K}\sigma_v^h - \nabla\cdot\mathbf{u}^h\right)\mathrm{d}\Omega + \int_\Omega h^2\left(\frac{a_2}{3K} + \frac{a_3}{G}\right)\nabla\sigma_v^h\cdot\nabla v^h\mathrm{d}\Omega = 0 \qquad \forall\ v^h \in \mathcal{S}_0^h. \tag{38}$$

The resulting linear system can be represented as

$$\begin{bmatrix} \mathrm{K}_2 & \mathrm{B}_1 \\ \mathrm{B}_1^T & -(\mathrm{A}_1 + \tilde{\mathrm{H}}) \end{bmatrix}\begin{bmatrix} \hat{\mathbf{u}} \\ \hat{\sigma}_v \end{bmatrix} = \begin{bmatrix} \mathbf{f}_u \\ 0 \end{bmatrix},$$

where stabilization term reads

$$\tilde{\mathrm{H}} = -\int_\Omega h^2\Big(\frac{a_2}{3K}+\frac{a_3}{G}\Big)\mathbf{G}^T\mathbf{G}\mathrm{d}\Omega. \tag{39}$$

6.3. Stabilized primal poroelasticity

In this case, the mass conservation equation does not depend on σ_v, therefore, we make $a_2 = a_3 = 0$ in Eq. (37) and substitute it into Eq. (9). After some manipulation, the stabilized weak form of the mass conservation equation reads

$$\int_\Omega q^h\left[\frac{1}{Q}\dot{p}^h + \alpha\nabla\cdot\dot{\mathbf{u}}^h\right]\mathrm{d}\Omega + \int_\Omega\left(a_1h^2\frac{\alpha^2}{G}\nabla\dot{p}^h + \frac{\mathbf{k}}{\mu}\nabla p^h\right)\cdot\nabla q^h\mathrm{d}\Omega = \mathbf{f}_p \quad \forall\ q^h\in\mathcal{P}_0^h.$$

The resulting fully discrete form is represented as,

$$\begin{bmatrix}\mathrm{K}_1 & \mathrm{B}_2\\ \mathrm{B}_2^T & -\big(\mathrm{A}_2+\Delta t\mathrm{F}+\tilde{\mathrm{F}}\big)\end{bmatrix}\begin{bmatrix}\hat{\mathbf{u}}\\ \hat{p}\end{bmatrix}^{n+1} = \begin{bmatrix}\mathbf{f}_u\\ \mathbf{f}_p\end{bmatrix} + \begin{bmatrix}0 & 0\\ \mathrm{B}_2^T & -\big(\mathrm{A}_2+\tilde{\mathrm{F}}\big)\end{bmatrix}\begin{bmatrix}\hat{\mathbf{u}}\\ \hat{p}\end{bmatrix}^{n}, \tag{40}$$

where

$$\tilde{\mathrm{F}} = -a_1\int_\Omega h^2\frac{\alpha^2}{G}\mathbf{G}^T\mathbf{G}\mathrm{d}\Omega. \tag{41}$$

6.4. Stabilized mixed poroelasticity

Substituting the full Eq. (37) into Eq. (20) leads to

$$\int_\Omega v^h\Big(\frac{1}{K}\sigma_v^h - \nabla\cdot\mathbf{u}^h\Big)\mathrm{d}\Omega + \int_\Omega\left[h^2\Big(\frac{a_2}{3K}+\frac{a_3}{G}\Big)\nabla\sigma_v^h - a_1h^2\frac{\alpha}{G}\nabla p^h\right]\cdot\nabla v^h\mathrm{d}\Omega = 0 \quad \forall\ v^h\in\mathcal{S}_0^h, \tag{42}$$

and into Eq. (21) results in

$$\int_\Omega q^h\left(\frac{1}{Q}\dot{p}^h + \alpha\nabla\cdot\dot{\mathbf{u}}^h\right)\mathrm{d}\Omega + \int_\Omega\left[\frac{\mathbf{k}}{\mu}\nabla p^h + a_1h^2\frac{\alpha^2}{G}\nabla\dot{p}_v^h - h^2\Big(\frac{a_2}{3K}+\frac{a_3}{G}\Big)\nabla\dot{\sigma}_v^h\right]\cdot\nabla q^h\mathrm{d}\Omega = \mathbf{f}_p, \quad \forall\ q^h\in\mathcal{P}_0^h. \tag{43}$$

Finally, the fully discrete stabilized mixed poroelasticity system of equations reads

$$\begin{bmatrix}\mathrm{K}_1 & \mathrm{B}_1 & \mathrm{B}_2\\ \mathrm{B}_1^T & -\big(\mathrm{A}_1+\check{\mathrm{H}}\big) & \check{\mathrm{H}}\\ \mathrm{B}_2^T & \check{\mathrm{F}} & -\big(\mathrm{A}_2+\Delta t\mathrm{F}+\tilde{\mathrm{F}}\big)\end{bmatrix}\begin{bmatrix}\hat{\mathbf{u}}\\ \hat{\sigma}_v\\ \hat{p}\end{bmatrix}^{n+1} = \begin{bmatrix}\mathbf{f}_u\\ 0\\ \mathbf{f}_p\end{bmatrix} + \begin{bmatrix}0 & 0 & 0\\ 0 & 0 & 0\\ \mathrm{B}_2^T & -\check{\mathrm{F}} & \mathrm{A}_2+\tilde{\mathrm{F}}\end{bmatrix}\begin{bmatrix}\hat{\mathbf{u}}\\ \hat{\sigma}_v\\ \hat{p}\end{bmatrix}^{n}, \tag{44}$$

where

$$\check{\mathrm{F}} = -\int_\Omega h^2\alpha\Big(\frac{a_2}{3K}+\frac{a_3}{G}\Big)\mathbf{G}^T\mathbf{G}\mathrm{d}\Omega \quad\text{and}\quad \check{\mathrm{H}} = -\int_\Omega h^2\alpha\frac{a_1}{G}\mathbf{G}^T\mathbf{G}\mathrm{d}\Omega.$$

Notice that generally $\check{\mathrm{H}}\neq\check{\mathrm{F}}^T$, hence the stabilized version of mixed poroelasticity produces a non-symmetric matrix. The resulting matrix is symmetric in only two situations:

1. $a_1 = 0$ in Eq. (42), and $a_2 = a_3 = 0$ in Eq. (43), implying $\check{\mathrm{F}} = \check{\mathrm{H}} = \mathbf{0}$; and
2. $a_1 = 1$ in Eq. (42), and $a_2 = 0$ and $a_3 = 1$ in Eq. (43), implying $\check{\mathrm{F}} = \check{\mathrm{H}}$.

7. Computation of parameter h

The parameter h, introduced in Section 6, is often referred to in the literature as a *characteristic length* of the element. Although it must reflect the size and shape of the element, its physical definition is not unique and different approaches have been proposed in the literature on how to compute h. For instance, Fig. 1 illustrates common options for a tetrahedral element, which include the radius or diameter of an inscribed sphere, and the diagonal of an equivalent cube with the same volume. These alternatives, however, stem from a purely geometrical interpretation of the parameter h.

In the present work, we propose to calculate the parameter h based on its role in Eqs. (31) and (32), which is to scale the effect of the Laplacian term in the approximation of a function at the integration point, $\psi(\mathbf{x}_c)$ (or $\mathbf{u}(\mathbf{x}_c)$ in Eq. 32). In the sequence, we present a procedure to automatically compute the parameter h in an optimal way, thus requiring no heuristic or user intervention in the definition of the stabilization term.

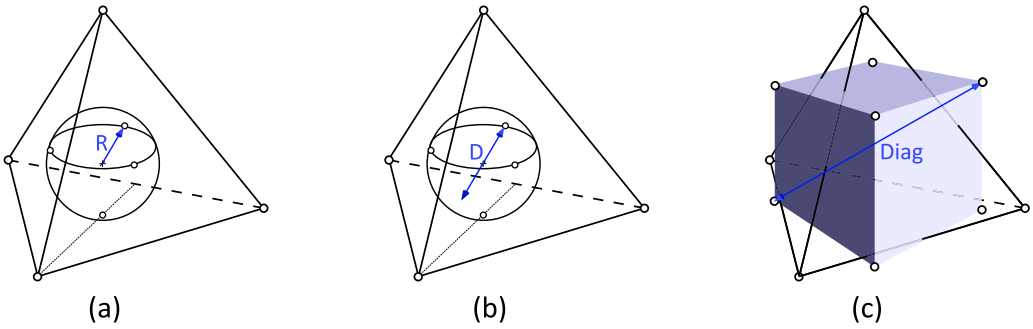

Fig. 1. Element characteristic length: (a) radius of inscribed sphere (h_iRad), (b) diameter of inscribed sphere, and (c) diagonal of an equivalent cube (h_Diag).

Table 1
Set of polynomial functions for a given tetrahedral element.

i	$\psi_i(\mathbf{x}_c)$	$\psi_i^h(\mathbf{x}_c)$	$\nabla^2\psi_i(\mathbf{x}_c)$	$r_i(h)$
0	$\psi_0(\mathbf{x}_c)$	$\psi_0^h(\mathbf{x}_c)$	$\nabla^2\psi_0(\mathbf{x}_c)$	$r_0(h)$
1	$\psi_1(\mathbf{x}_c)$	$\psi_1^h(\mathbf{x}_c)$	$\nabla^2\psi_1(\mathbf{x}_c)$	$r_1(h)$
⋮	⋮	⋮	⋮	⋮
m	$\psi_m(\mathbf{x}_c)$	$\psi_m^h(\mathbf{x}_c)$	$\nabla^2\psi_m(\mathbf{x}_c)$	$r_m(h)$

7.1. Optimization procedure

The strategy consists of calculating the value of h that gives the most accurate approximations for a set of polynomial functions $\psi_i(\mathbf{x})$ of degree N, for $i \in [0, m]$ with m denoting the number of polynomial functions considered. We express a general polynomial function as

$$\psi_i(\mathbf{x}) = \sum_{p=0}^{N} A_{ip}(x + a_{ip})^p + B_{ip}(y + b_{ip})^p + C_{ip}(z + c_{ip})^p, \tag{45}$$

where we arbitrarily choose A_{ip}, B_{ip}, and C_{ip} as random values between -2 and 2 , and a_{ip}, b_{ip}, and c_{ip} as random values between -1 and 1.

The exact Laplacian of ψ_i is given by

$$\nabla^2\psi_i(\mathbf{x}) = \sum_{p=2}^{N} \left[p(p-1)A_{ip}(x + a_p)^{p-2} + p(p-1)B_{ip}(y + b_p)^{p-2} + p(p-1)C_{ip}(z + c_p)^{p-2}\right]. \tag{46}$$

In this work, the polynomial order is chosen to be $N = 2$, resulting in constant Laplacian inside the element. From our experience, higher polynomial degrees ($N \geq 3$) do not significantly change the results, because the mesh is usually sufficiently refined such that the solution (function) does not change significantly inside the element.

For a given tetrahedron with centroid coordinates $\mathbf{x}_c$, we define a residual equation as

$$r_i(h) = \psi_i^h(\mathbf{x}_c) - h^2\nabla^2\psi_i(\mathbf{x}_c) - \psi_i(\mathbf{x}_c). \tag{47}$$

where the term $\psi_i^h(\mathbf{x}_c) - h^2\nabla^2\psi_i(\mathbf{x}_c)$ represents the approximate function value at $\mathbf{x}_c$, and $\psi_i(\mathbf{x}_c)$ is the exact function value. Notice that $\psi_i^h(\mathbf{x}_c)$ represents the average value of ψ at the vertices of the tetrahedron.

The values of $r_i(h)$ computed by Eq. (47) for a family of m polynomials in a given tetrahedron are collected in a table structured as Table 1.

Next, we define a total residual equation as

$$R(h) = \sum_{i=0}^{m} |r_i(h)|. \tag{48}$$

The goal is to find the optimum value of h for which $R(h)$ is minimum. In this manner, the h parameter for a certain element e is obtained by solving the following optimization problem

$$h_e^* = \arg\min_{h\in\mathbb{R}^+} R(h).$$

Unlike the degree N of the polynomial functions, the number of functions, m, can significantly impact the results of h_e^*. Consider a typical tetrahedral element as the one illustrated on the left of Fig. 2. The right graph of this same figure shows the values of h_e^* obtained from the optimization procedure, as described before, for increasingly larger values of m. It suggests that the number of

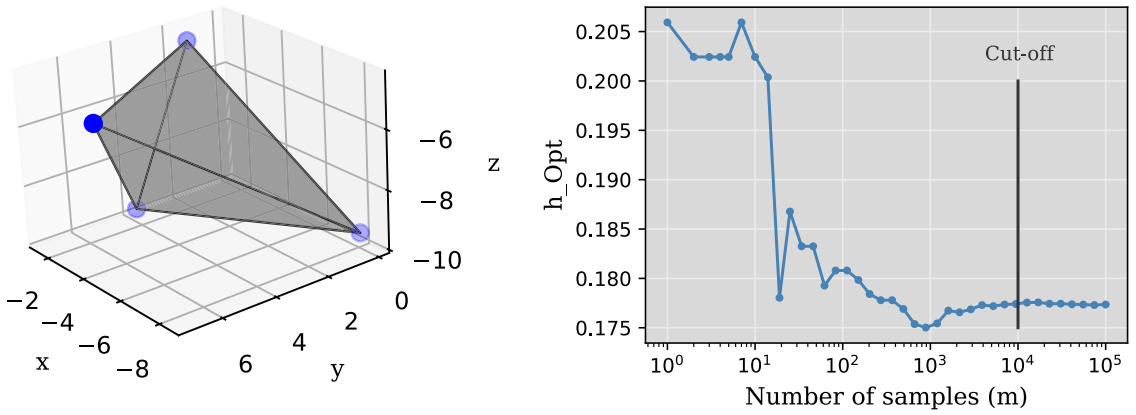

Fig. 2. Tetrahedral element (left) and convergence of optimal characteristic length with the number of samples (right).

Table 2
Datasets for n tetrahedral elements: (left) original and (right) standard element dimensions.

e	$\mathbf{x}_{e,1}$	$\mathbf{x}_{e,2}$	$\mathbf{x}_{e,3}$	$\mathbf{x}_{e,4}$	h_e^*		e	$\tilde{\mathbf{x}}_{e,1}$	$\tilde{\mathbf{x}}_{e,2}$	$\tilde{\mathbf{x}}_{e,3}$	$\tilde{\mathbf{x}}_{e,4}$	$\tilde{h}_e^*$
0	$\mathbf{x}_{0,1}$	$\mathbf{x}_{0,2}$	$\mathbf{x}_{0,3}$	$\mathbf{x}_{0,4}$	h_0^*		0	$\tilde{\mathbf{x}}_{0,1}$	$\tilde{\mathbf{x}}_{0,2}$	$\tilde{\mathbf{x}}_{0,3}$	$\tilde{\mathbf{x}}_{0,4}$	$\tilde{h}_0^*$
1	$\mathbf{x}_{1,1}$	$\mathbf{x}_{1,2}$	$\mathbf{x}_{1,3}$	$\mathbf{x}_{1,4}$	h_1^*	→	1	$\tilde{\mathbf{x}}_{1,1}$	$\tilde{\mathbf{x}}_{1,2}$	$\tilde{\mathbf{x}}_{1,3}$	$\tilde{\mathbf{x}}_{1,4}$	$\tilde{h}_1^*$
⋮	⋮	⋮	⋮	⋮	⋮		⋮	⋮	⋮	⋮	⋮	⋮
n	$\mathbf{x}_{n,1}$	$\mathbf{x}_{n,2}$	$\mathbf{x}_{n,3}$	$\mathbf{x}_{n,4}$	h_n^*		n	$\tilde{\mathbf{x}}_{n,1}$	$\tilde{\mathbf{x}}_{n,2}$	$\tilde{\mathbf{x}}_{n,3}$	$\tilde{\mathbf{x}}_{n,4}$	$\tilde{h}_n^*$

samples (or polynomial functions) should be larger than 1000, after which h_e^* converges to an approximately constant value. To be on the safe side, we adopt $m = 10,000$.

7.2. Machine learning model

Although the optimization procedure described above can be performed just once for a given mesh, it can be considerably expensive, especially for fine meshes and large values of m. For this reason, we propose to replace this procedure by a machine learning model, which is trained off-line and can immediately predict the optimal h value for any tetrahedron of the mesh. In what follows, we describe the process to dataset creating and machine learning training.

The optimization procedure described in Section 7.1 is performed for many different tetrahedral elements, resulting in the dataset represented in the leftmost frame of Table 2, where $\mathbf{x}_{i,e}$ represents the coordinates x, y and z of the i^{th} vertex of the element e. In the present work, we generate such dataset by considering the elements originating from different discretizations created in Gmsh [53]. The number of sample elements n is approximately 200,000. This dataset, however, is not suitable for the machine learning training because the parameter h_e^* should not depend on the spatial position of the element, but only on the element aspect ratio. To circumvent this issue, we move the element to the origin of the coordinate system and rescale it to a standard size before training the ML model, as illustrated in Fig. 3. This procedure can be summarized as follows:

1. Calculate the centroid coordinates of the element as $\mathbf{x}_{e,c} = \frac{1}{4}\sum_{i=1}^{4} \mathbf{x}_{e,i}$;
2. Move the element centroid to the origin of the coordinate system, i.e., $\mathbf{x}_{e,i} \leftarrow \mathbf{x}_{e,i} - \mathbf{x}_{e,c}$;
3. Calculate the maximum edge length, L_e of the element;
4. Rescale the element by dividing all vertex coordinates by L_e, i.e., $\tilde{\mathbf{x}}_{i,e} = \mathbf{x}_{i,e}/L_e$;
5. Rescale h_e^* to the standard dimension, i.e., $\tilde{h}_e^* = h_e^*/L_e$.

By performing these operations for every element in the dataset, the transformed dataset presented in the rightmost frame of Table 2 is obtained. The transformed dataset is now suitable to train the machine learning model. For this purpose, the dataset is randomly split into training and test sets and a machine learning model is trained to regress the values of $\tilde{h}_e^*$ based on the vertex coordinates $\tilde{\mathbf{x}}_{e,i}$ of the standard element $\tilde{e}$. The machine learning model adopted is the histogram-based gradient boosting algorithm (HistGradientBoostingRegressor) as implemented in Scikit-learn [54]. The trained ML model consists of a function $F_{ML} : \mathbb{R}^{4\times3} \to \mathbb{R}$ that receives the spatial coordinates of all vertices of an element $\tilde{\mathbf{e}}$ and returns a prediction of $\tilde{h}_e^*$. For a given element e, with vertex coordinates $\mathbf{x}_{e,1}$, $\mathbf{x}_{e,2}$, $\mathbf{x}_{e,3}$, and $\mathbf{x}_{e,4}$, the procedure is as follows:

1. Calculate $\mathbf{x}_{e,c} = \frac{1}{4}\sum_{i=1}^{4} \mathbf{x}_{e,i}$;
2. Move the element to the origin, $\mathbf{e}' = [\mathbf{x}_{e,1} - \mathbf{x}_{e,c}, \mathbf{x}_{e,2} - \mathbf{x}_{e,c}, \mathbf{x}_{e,3} - \mathbf{x}_{e,c}, \mathbf{x}_{e,4} - \mathbf{x}_{e,c}]$ (see Fig. 3b);
3. Calculate the maximum edge length L_e;
4. Rescale the element to the standard size, $\tilde{\mathbf{e}} = \mathbf{e}/L_e = [\tilde{\mathbf{x}}_{e,1}, \tilde{\mathbf{x}}_{e,2}, \tilde{\mathbf{x}}_{e,3}, \tilde{\mathbf{x}}_{e,4}]$ (see Fig. 3c);

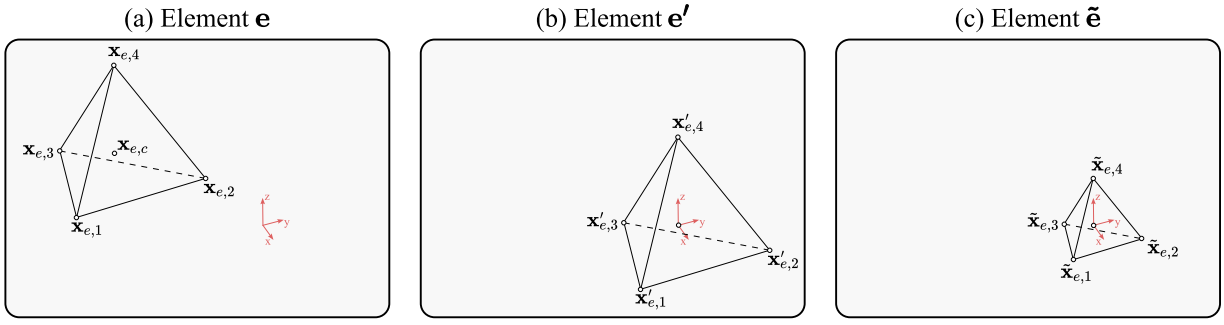

Fig. 3. Element transformation steps: (a) original dimensions and position; (b) Repositioning to the origin; (c) Rescaling to a standard dimension.

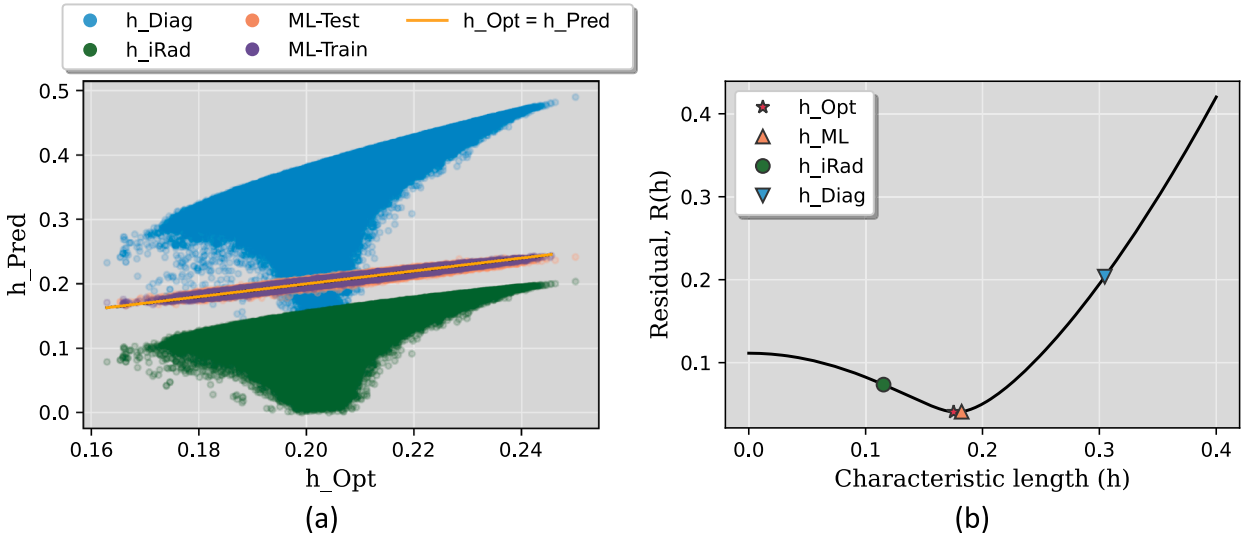

Fig. 4. (Left) Comparison of predicted h_Opt obtained with the machine learning model in the training and test sets, and inscribed radius and equivalent diagonal. (Right) Residual for different calculations of parameter h considering the tetrahedral element shown in Fig. 2a.

5. Use the trained ML model to predict h in the standard element size, i.e., $\tilde{h}_e \leftarrow F_{ML}(\tilde{\mathbf{e}})$;
6. Rescale back to the original element size, i.e., $h_e \leftarrow \tilde{h}_e * L_e$.

The results of h^*_{pred} on the training and testing sets are shown in Fig. 4a. For comparison, the values obtained with the inscribed radius (h_iRad) and equivalent diagonal (h_Diag), both illustrated in Fig. 1, are also shown in Fig. 4a. It can be observed that h_Diag mostly over estimate the characteristic length, compared to the optimal characteristic length (h_Opt). On the other hand, h_iRad consistently underestimate the h_Opt. This can also be observed in Fig. 4b, where the points h_Opt, h_ML, h_iRad, and h_Diag are shown on top of the total residue function (Eq. 48) for the element depicted in Fig. 2. Also worth noting, is that the ML prediction of the optimal h^* value (h_ML) is very close to h_Opt. Therefore, h_Opt is disregarded from this work, and only h_ML is considered for the comparisons with h_iRad and h_Diag.

8. Stability analysis

Similarly to most stabilization strategies, the approach proposed here introduces numerical diffusion to mitigate the oscillatory behavior of the solution. In this subsection, we focus on evaluating whether the amount of numerical diffusion applied is excessive or insufficient. Specifically, we restrict our analysis to the linear elasticity problem, where the primary unknowns are displacement and mean stress, and consider the limit of an incompressible medium (i.e., as Poisson's ratio $\nu \to 0.5$). To assess the quality of the stabilization, we follow the methodology outlined in [51], which involves analyzing the square root of the smallest non-zero eigenvalue of the scaled Schur complement. This quantity is the numerical evaluation of the constant appearing in the inf-sup condition, whose independence from the mesh size is critical for ensuring the stability of the method. The procedure for this evaluation is described in detail below.

Let us consider the linear elasticity model for incompressible solids, that is,

$$\begin{cases} \nabla \cdot \left[2G\left(\boldsymbol{\varepsilon} - \frac{1}{3}\varepsilon_v \mathbf{I}\right)\right] + \nabla \sigma_v = \mathbf{b}, \\ \nabla \cdot \mathbf{u} = 0. \end{cases} \tag{49}$$

The corresponding weak form is given by:

$$\begin{cases} a(\mathbf{u}, \mathbf{w}) + b(\mathbf{w}, \sigma_v) = f(\mathbf{u}) & \forall \quad \mathbf{w} \in \mathcal{U}_0, \\ b(\mathbf{u}, v) = 0 & \forall \quad v \in \mathcal{S}_0, \end{cases} \tag{50}$$

where the bilinear forms are defined as:

$$a(\mathbf{u}, \mathbf{w}) = \int_\Omega 2G\boldsymbol{\varepsilon}(\mathbf{u}) : \boldsymbol{\varepsilon}(\mathbf{w}) d\Omega - \frac{2}{3}\int_\Omega G\varepsilon_v(\mathbf{u}) \nabla \cdot \mathbf{w} d\Omega, \tag{51}$$

$$b(\mathbf{w}, v) = -\int_\Omega v \nabla \cdot \mathbf{w} d\Omega, \tag{52}$$

and the linear form is given by $f(\mathbf{w}) = \int_\Omega \mathbf{b} \cdot \mathbf{w} d\Omega$.

After introducing the stabilization, the modified weak formulation becomes:

$$\begin{cases} a(\mathbf{u}, \mathbf{w}) + b(\mathbf{w}, \sigma_v) = f(\mathbf{u}) & \forall \quad \mathbf{w} \in \mathcal{U}_0, \\ b(\mathbf{u}, v) + c(\sigma_v, v) = 0 & \forall \quad v \in \mathcal{S}_0, \end{cases} \tag{53}$$

with the stabilization term defined as:

$$c(\sigma_v, v) = \int_\Omega \frac{h^2}{G} \nabla \sigma_v \cdot \nabla v d\Omega. \tag{54}$$

The Jacobian matrix, obtained by discretizing the system in (53), is:

$$\mathrm{J} = \begin{bmatrix} \mathrm{K}_2 & \mathrm{B}_1 \\ \mathrm{B}_1^T & -\tilde{\mathrm{H}} \end{bmatrix} \tag{55}$$

Finally, the mass matrix in the $\mathcal{S}_0$ space, which will be utilized later in the analysis, corresponds to the discretization of the following form, appropriately scaled by a stiffness constant:

$$m(\sigma_v, v) = \int_\Omega \frac{1}{2G} \sigma_v v d\Omega. \tag{56}$$

Following the approach developed by Elman et al. [55, Chapter 5], an alternative method to verify the inf-sup condition

$$0 < \gamma \leq \inf_{v \in \mathcal{S}_0} \sup_{\mathbf{w} \in \mathcal{U}_0} \frac{|b(\mathbf{w}, v)|}{\|\mathbf{w}\|_{1,\Omega} \|v\|_{0,\Omega}}, \tag{57}$$

with γ independent of h, is to examine the discrete version of the operators appearing in (57). Specifically, the generalized inf-sup constant is given by:

$$\delta^2 = \min_{v^h \in \mathcal{S}_0^h} \frac{\langle \left(\mathrm{B}_1^T \mathrm{K}_2^{-1} \mathrm{B}_1 + \tilde{\mathrm{H}}\right) \hat{v}, \hat{v} \rangle}{\langle \mathrm{Q}\hat{v}, \hat{v} \rangle}, \tag{58}$$

where $v^h = \mathbf{N}(\mathbf{x})\hat{v}$. This indicates that stability is determined by the smallest nonzero eigenvalue of the scaled Schur complement $\mathrm{Q}^{-1}\left(\mathrm{B}_1^T \mathrm{K}_2^{-1} \mathrm{B}_1 + \tilde{\mathrm{H}}\right)$, associated with (55), where Q is the mass matrix, derived from discretization of the term in (56).

To explore the relationship between γ and δ, a new functional is introduced:

$$s(v) = \max_{\mathbf{w} \in \mathcal{U}_0} \frac{|b(\mathbf{w}, v)|}{\|\nabla \mathbf{w}\|} + c(v, v)^{1/2}, \tag{59}$$

and with this, the definition of *uniform stability* is satisfied when:

$$s(v) \geq \delta \|v\| \quad \forall v \in \mathcal{S}_0, \tag{60}$$

with δ independent of h. A more detailed discussion of this topic is beyond the scope of this work; the interested reader is referred to Elman et al. [55] and the references therein for further information.

This process is performed for different mesh refinements and for the three characteristic lengths considered h_iRad, h_Diag and h_ML, and the non-stabilized version, h_0. For this analysis, a simple unit cube is considered in which one face is fully locked, and the opposite face is subjected to a compressive load. The geometry is discretized using unstructured tetrahedral meshes with 5 levels of refinement. The details of each mesh are provided in Table 3. The results obtained from this analysis are shown in Fig. 5.

Ideally, the square root of the smallest non-zero eigenvalue should be 1, irrespective of the grid refinement (or element size), which indicates a completely stable pair [55]. Fig. 5 shows that this is not the case for the non-stabilized P1P1, for which the smallest non-zero eigenvalue of the scaled Schur complement uniformly decreases with the grid size. All the stabilized alternatives provide a stable smallest non-zero eigenvalue close 1, with the h_ML choice being the closest to the unitary value.

Table 3
Refinement levels of the unitary cube.

h	nodes	elements	n_1	n_2	n_t
1.00000	14	24	42	14	56
0.63719	45	100	135	45	180
0.37760	209	627	627	209	836
0.23748	1083	4279	3249	1083	4332
0.12214	5940	27,292	17,820	5940	23,760

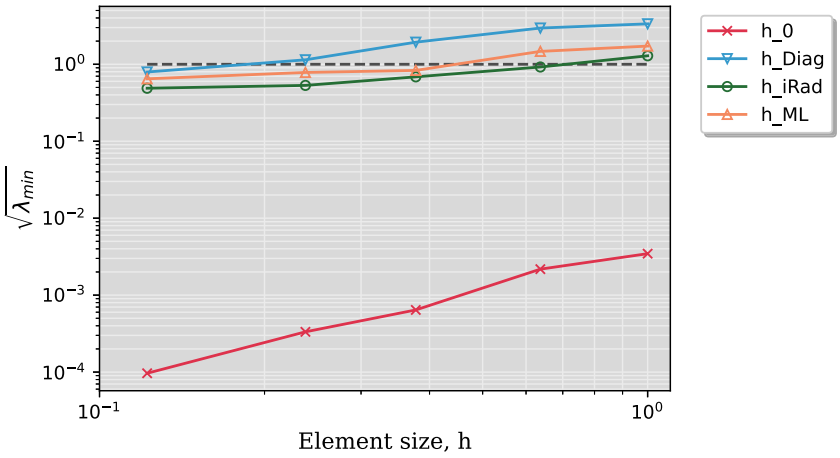

Fig. 5. Stability analysis for the mixed P1P1 formulation of the linear elasticity model in the incompressibility limit.

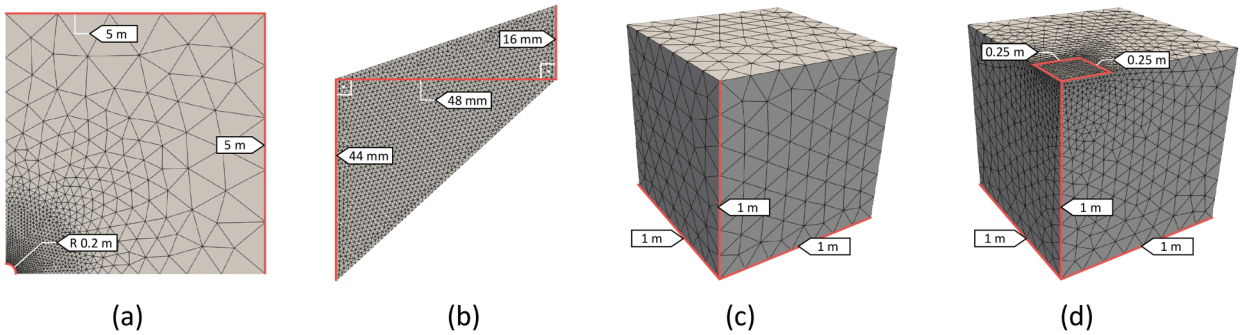

Fig. 6. Geometries and grids used for the test cases. (a) Plate hole: 2640 vertices, 9944 tetras (width = 0.2 m). (b) Cook's membrane: 3835 vertices, 11,120 tetras (width = 1 mm). (c) Mandel's problem: 7353 vertices, 36,688 tetras. (d) Strip footing: 2051 vertices, 8492 tetras.

9. Results

Four different problems are considered to test the stabilization strategies presented in this paper. The first two problems consist of the classical plate with circular hole and Cook's membrane problems, which are intended to test the linear elasticity model. For poroelasticity, the solution for Mandel's and strip footing problems are investigated. Fig. 6 shows the geometries and meshes adopted for each problem. These test cases are described in the following subsections. In all test cases, the nodal values of the mean stress will be evaluated. For the mixed formulations, the nodal mean stress field directly comes from the solution vector. In contrast, in the primal formulations, the mean stresses are calculated at the elements, based on the nodal displacements $\mathbf{u}^h$, and interpolated to the nodal points by simple volume-weighted average.

9.1. Linear elasticity problems

The linear elasticity model is used here to investigate the conditions in which mean stress oscillations appear, and how the proposed stabilization scheme performs with respect to the different h parameter calculations, i.e., h_iRad, h_Diag, h_ML, and h_0 (no stabilization). The test cases and numerical experiments are described below.

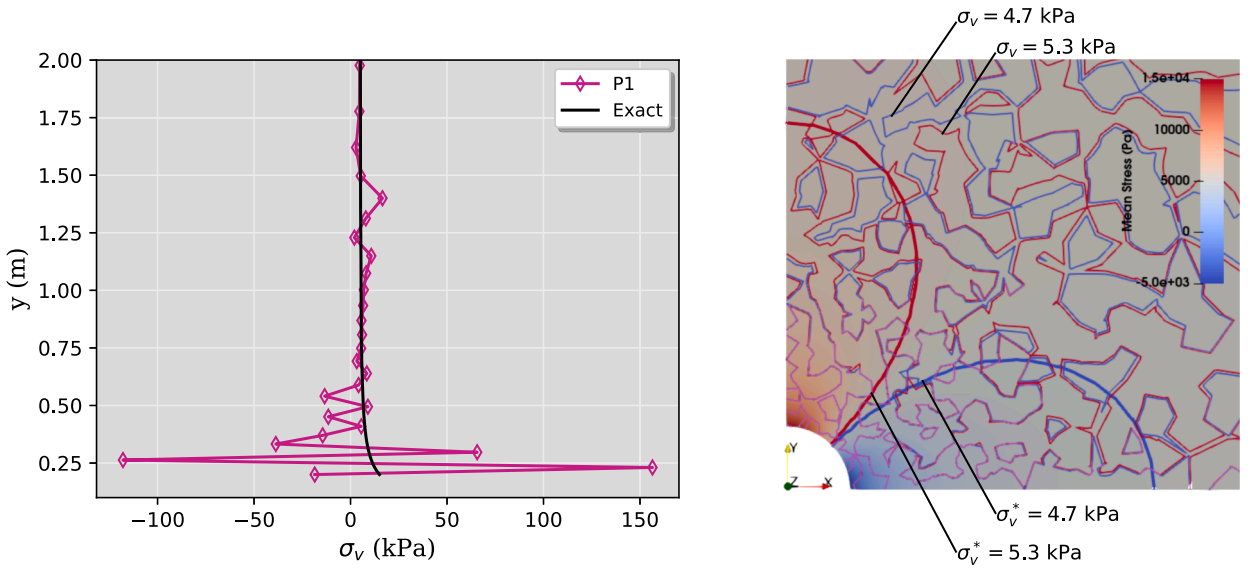

Fig. 7. Plate hole results for P1 formulation. (Left) Volumetric stress along the line $x = z = 0$. (Right) Exact volumetric stress field, exact isolines for 4.7 and 5.3 kPa and the corresponding numerical isolines obtained with the P1 formulation.

9.1.1. Plate hole

The plate with a circular hole is a classical problem in linear elasticity to study stress concentrations, and its analytical solution dates back to 1898 [56]. The problem consists of an infinite plate with a circular hole of radius R, subjected to a traction stress σ in one direction, and subjected to plane strain condition. Although the stresses in the plane directions (i.e., σ_{rr} and $\sigma_{\theta\theta}$) do not depend on the elastic properties, the out-of-plane stress (σ_{zz}) does depend on Poisson's ratio. Consequently, the mean stress field also depends on Poisson's ratio, ν, and its exact solution is shown in Appendix B. In this work, a traction stress of $\sigma = 10$ kPa is applied in the horizontal direction (that is, the right boundary), the top and circular boundaries are stress free, and zero normal displacement is imposed on all the remaining boundaries. Additionally, a Poisson's ratio of $\nu = 0.4999$ is adopted in order to reproduce a nearly incompressible solid, thus posing a challenging restriction to the mean stress equation (saddle point problem). The geometry adopted consists of a finite square of 5 m and a circular hole of $R = 0.2$ m, as shown in Fig. 6. A mesh refinement was applied to the region between $0.2\text{ m} \leq R \leq 1.4$ m.

This problem is solved with the primal formulation using P1 elements, with the mixed formulation using P1P1 (with and without stabilization) and a mixed P2P1 formulation, which is known to be LBB-stable. As expected from the nearly incompressible conditions, the solution obtained with the primal P1 formulation produces a highly oscillatory mean stress field, as shown in Fig. 7. The left diagram of this figure presents the numerical and analytical mean stress fields along the vertical line at $x = z = 0$, where the negative values clearly indicate non-physical results. The right graph shows a plot of the exact mean stress field. For comparison, we plot the exact isolines for $\sigma_v^* = 4.7$ kPa and $\sigma_v^* = 5.3$ kPa, and the corresponding numerical results.

The solutions obtained with the mixed formulations are presented in Fig. 8, which shows the same types of results as in Fig. 7. In the legend, P1P1_h_0 refers to the P1P1 formulation with no stabilization ($h = 0$), and P1P1_h_ML, P1P1_h_iRad and P1P1_h_Diag refer to the stabilized P1P1 formulations with the h parameters calculated by the machine learning model (see Section 7.2), inscribed radius and equivalent diagonal (see Fig. 1). In all cases, it was considered $a_2 = a_3 = 1$ in Eq. (39). Fig. 8 reveals that the mixed formulation P1P1 without stabilization significantly reduces the mean stress oscillations when compared to the primal P1 formulation (Fig. 7), although they are not completely removed. The stabilized versions, however, effectively remove spurious oscillations. The P1P1_h_ML, in particular, provides a very accurate prediction of the maximum mean stress, at the top of the circular hole.

The H^1-norm of the mean stress error field can be computed based on the available exact solution. To comply with the infinite plate assumption, the error of the numerical solution is calculated only in the circular region between $0.2\text{ m} \leq R \leq 1.4$ m, which is relatively far from the borders. The results in the left graph of Fig. 9 show that the H^1-norm associated the P1 formulation is much higher than for the mixed formulations. The errors norms obtained with P1P1 and P2P1 formulations are all comparable to each other, with the non-stabilized P1P1_h_0 error being slightly higher (41820). Nevertheless, the non-stabilized P1P1 formulation produces a physically inconsistent (i.e., oscillatory) solution. Moreover, P1P1_h_Diag and P1P1_h_ML provide slightly better results than P2P1. When these results are analyzed together with the number of unknowns of each method, shown in right graph of Fig. 9, it becomes clear that the stabilized P1P1 formulations definitely provide the most accurate results with the lowest computation cost. This is because the number of nodal displacements in the P2P1 formulation is much higher than for the P1P1 and P1 formulations.

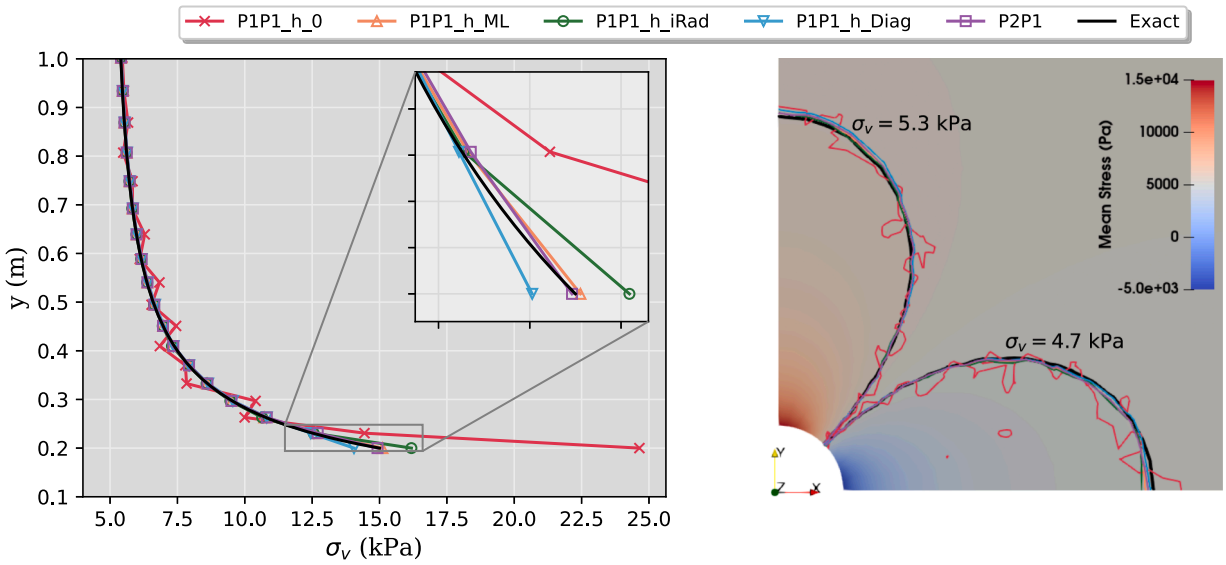

Fig. 8. Plate hole results for P1P1 formulation considering different characteristic lengths for stabilization. (Left) Volumetric stress along the line $x = z = 0$. (Right) Exact volumetric stress field, exact isolines for 4.7 and 5.3 kPa and the corresponding numerical isolines obtained with different choices of characteristic lengths.

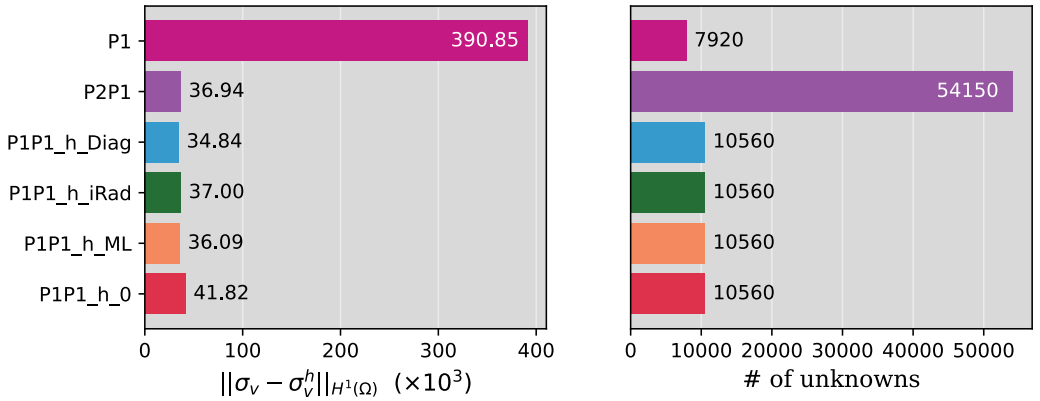

Fig. 9. (Left) H^1-norm of the error, and (right) the corresponding number of degrees of freedom.

9.1.2. Cook's membrane

Cook's membrane is a challenging problem designed to test volumetric locking due to shear stresses in (nearly) incompressible solids. Problem geometry and computational grid are shown in Fig. 6b. The left boundary is fixed and a shear stress $\tau_{yy} = 10$ kPa is imposed on the right boundary. The out-of-plane surfaces (z direction) are prevented from normal displacement. Fig. 10 shows the results obtained with the P1P1 mixed formulations, with and without stabilization, and the P2P1 formulation. The left graph shows the mean stress profile along the left boundary of the geometry. As expected, strong oscillations are observed when no stabilization is employed for the P1P1 formulation. All stabilization versions are able to eliminate non-physical oscillations and produce remarkably similar results, with P1P1h_inR and P2P1 agreeing more with each other at the top-left corner of the geometry. On the right graph of Fig. 10, mean stress isolines for all formulations are shown to have very good agreement, except for the non stabilized mixed formulation P1P1h0.

The next analysis has three goals. The first one is to test the effectiveness of the proposed stabilization at removing both Gibbs and saddle-point oscillations. For this purpose, Cook's membrane problem is solved for Poisson's ratios of 0.0, 0.3, and 0.4999. The second goal is to compare the results of the primal (P1) and mixed (P1P1) formulations for the 3 values of Poisson's ratio. Finally, the third goal is to test the inclusion of the different terms in Eq. (37) by choosing different values for a_2 and a_3 (recalling that a_1 is always zero for linear elasticity). Fig. 11 shows the mean stress profiles along the vertical line on the right boundary obtained with the P1P1 formulation. Light to mild oscillations are observed when $\nu = 0.0$ and $\nu = 0.3$ for the non-stabilized version ($a_2 = a_3 = 0$), which are associated with the Gibbs phenomenon, while strong saddle-point oscillations are observed for $\nu = 0.4999$. For this case (nearly incompressible solid), the bulk modulus increases to infinity, which explains why the results of $a_2, a_3 = 1, 0$ are equal to $a_2, a_3 = 0, 0$.

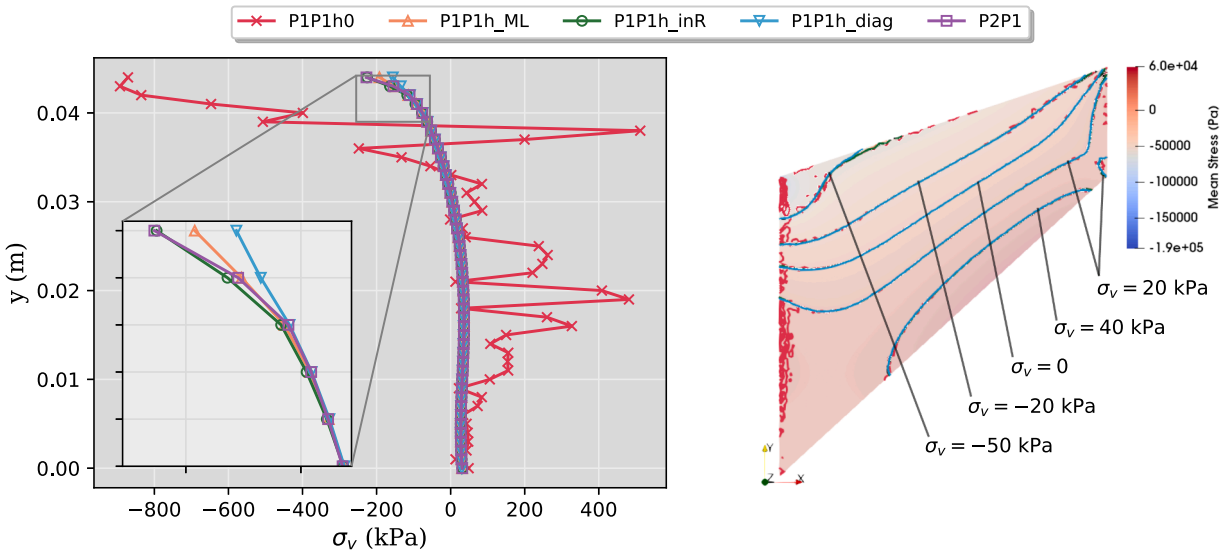

Fig. 10. Cook's membrane results for P1P1 formulation considering different characteristic lengths for stabilization. (Left) Volumetric stress along the line $x = z = 0$. (Right) Volumetric stress field obtained with P2P1 formulation, and isolines.

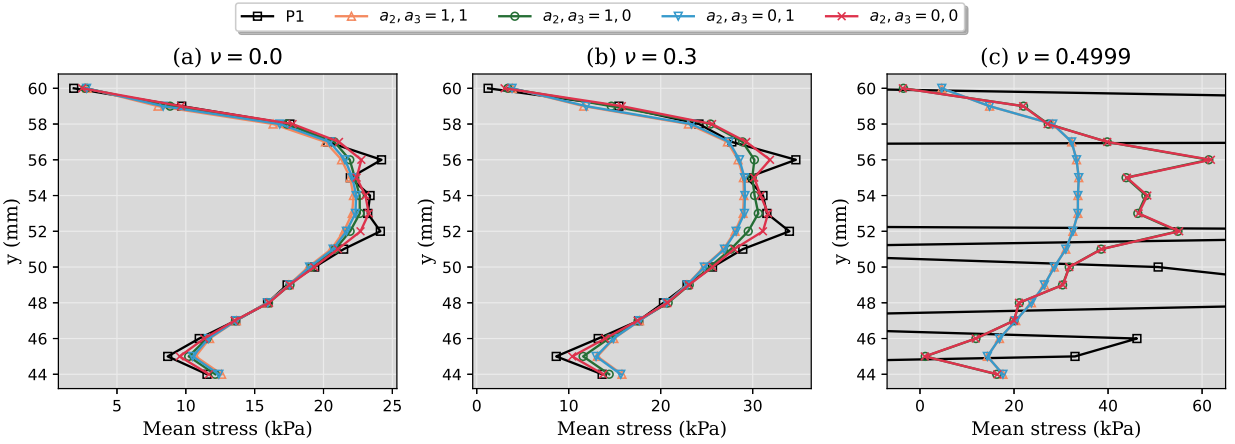

Fig. 11. Cook's membrane: mean stress profile along the loading boundary obtained with the P1 formulation and the P1P1 formulations considering different stabilization terms. Three different values are considered for Poisson's ratio.

The analysis of the results for $\nu = 0.0$ and $\nu = 0.3$ suggests that including the term $1/G$ ($a_3 = 1$) in Eq. (37) is more important than term $1/(3K)$ ($a_2 = 1$). Regarding the second goal, Fig. 11c shows that the primal P1 formulation is very sensitive to the nearly-incompressibility conditions, as expected. For the same case (Fig. 11c), the mixed P1P1 with no stabilization (i.e., $a_2 = a_3 = 0$) is less sensitive than the primal formulation, but is still highly oscillatory. In the cases where $\nu = 0.0$ and $\nu = 0.3$, the oscillations are only due to the Gibbs phenomenon. Fig. 11a and b show that, in the presence of Gibbs oscillations, the difference between P1 and P1P1 formulations is not as significant as for the nearly incompressible case.

9.2. Coupled poroelasticity problems

This subsection describes the test cases used to investigate the performance of the proposed stabilization strategy for coupled poroelasticity problems. The test cases are presented below.

9.2.1. Stabilization terms

In this section, we investigate the use of different terms in the stabilized displacement approximation (Eq. 37), which is repeated here for convenience, i.e.,

$$\mathbf{u} \approx \mathbf{u}^h - a_1 h^2 \frac{\alpha}{G} \nabla p^h + h^2 \left(\frac{a_2}{3K} + \frac{a_3}{G} \right) \nabla \sigma_v^h.$$

Table 4
Terms considered in the stabilized **u** approximation and the corresponding labels and stabilization matrices.

Label	Eq. (42)			Eq. (43)			$\tilde{\mathbf{H}}$	$\check{\mathbf{H}}$	$\tilde{\mathbf{F}}$	$\check{\mathbf{F}}$
$a_1a_2a_3\_a_1a_2a_3$	a_1	a_2	a_3	a_1	a_2	a_3				
111_100	1	1	1	1	0	0	$R=\frac{1}{3K}+\frac{1}{G}$	$R=\alpha\frac{1}{G}$	$R=\frac{\alpha^2}{G}$	$R=\alpha\left(\frac{1}{3K}+\frac{1}{G}\right)$
101_100	1	0	1	1	0	0	$R=\frac{1}{G}$	$R=\alpha\frac{1}{G}$	$R=\frac{\alpha^2}{G}$	0
110_100	1	1	0	1	0	0	$R=\frac{1}{3K}$	$R=\alpha\frac{1}{G}$	$R=\frac{\alpha^2}{G}$	0
011_100*	0	1	1	1	0	0	$R=\frac{1}{3K}+\frac{1}{G}$	0	$R=\frac{\alpha^2}{G}$	0
111_111	1	1	1	1	1	1	$R=\frac{1}{3K}+\frac{1}{G}$	$R=\alpha\frac{1}{G}$	$R=\frac{\alpha^2}{G}$	$R=\alpha\left(\frac{1}{3K}+\frac{1}{G}\right)$
111_101*	1	1	1	1	0	1	$R=\frac{1}{3K}+\frac{1}{G}$	$R=\alpha\frac{1}{G}$	$R=\frac{\alpha^2}{G}$	$R=\alpha\frac{1}{G}$
111_110	1	1	1	1	1	0	$R=\frac{1}{3K}+\frac{1}{G}$	$R=\alpha\frac{1}{G}$	$R=\frac{\alpha^2}{G}$	$R=\frac{1}{3K}$

Table 5
Poroelastic properties.

Property	Symbol	Value	Unit
Poisson's ratio	ν	0.3	-
Shear modulus	G	9.79	MPa
Solid compressibility	c_s	2.06×10^{-10}	Pa^{-1}
Porosity	ϕ	0.48	-
Permeability	k	3.62×10^{-12}	m^2
Fluid compressibility	c_f	4.44×10^{-10}	Pa^{-1}
Viscosity	μ	0.001	$Pa{\cdot}s^{-1}$

For this investigation, we consider Mandel's problem and the strip footing (both of them are properly described in Sections 9.2.2 and 9.2.3, respectively).

We emphasize that the stabilized **u** approximation is introduced in the mean stress equation (Eq. 20) and the mass balance for the fluid phase (Eq. 21), and different stabilization terms (i.e., a_1, a_2 and a_3) can be chosen in each of these two equation. In a general form, the stabilization terms in Eqs. (40) and (44) can be represented as

$$\mathbf{R}=\int_\Omega h^2 R\mathbf{G}^T\mathbf{G}\,\mathrm{d}\Omega \quad \text{where} \quad \begin{cases} \mathbf{R}=\tilde{\mathbf{H}}, & \text{if} \quad R=\frac{a_2}{3K}+\frac{a_3}{G}; \\ \mathbf{R}=\check{\mathbf{H}}, & \text{if} \quad R=a_1\frac{\alpha}{G}; \\ \mathbf{R}=\tilde{\mathbf{F}}, & \text{if} \quad R=a_1\frac{\alpha^2}{G}; \\ \mathbf{R}=\check{\mathbf{F}}, & \text{if} \quad R=\alpha\left(\frac{a_2}{3K}+\frac{a_3}{G}\right). \end{cases}$$

In this manner, the stabilization strategies considered for testing can be summarized as in Table 4. There are many other possible combinations, but only the best and most meaningful ones are considered here. Also, notice that only the options 011_100 and 111_101 result in a symmetric matrix.

These strategies are employed to analyze the results of Mandel's poroelastic slab and the strip footing problems, both described in following subsections. The pore pressure and mean stress profiles obtained for these two problems are shown in Fig. 12. The results reveal that including all terms into the stabilized **u** approximation (111_111) for both Eqs. (20) and (21) is not a good practice as it does not completely suppress oscillations. The options 011_100 and 111_101, both of which result in symmetric matrices, also do not produce good results. Comparing 111_100, 111_101, 111_110 and 111_111 reveals that including the term $\frac{1}{3K}\nabla\sigma_v$ into the stabilized **u** approximation in Eq. (21) is beneficial to the numerical solution, whereas the term $\frac{1}{G}\nabla\sigma_v$ is not. As a general rule, the pore pressure term should always be kept in both Eqs. (20) and (21). The mean stress terms should also be avoided for Eq. (21), although 111_110 does produce a good result. Lastly, comparing 111_100 and 101_100 shows that using $\frac{1}{G}\nabla\sigma_v$ in addition to $\frac{1}{3K}\nabla\sigma_v$ makes the model slightly more dissipative.

9.2.2. Mandel's problem

The unitary cube shown in Fig. 6 is used for this test case. Zero normal displacements are prescribed on $x=0$, $y=0$, $z=0$ and $z=1$, and zero pressure is imposed on $x=1$. On the top boundary, a time dependent normal displacement is imposed according to the analytical solution of Mandel's problem, which can be found, for instance, in Verruijt [57]. At $t=0$, all displacements and pressures are zero. We employ 100 time steps logarithmically spaced between $10^{-3.35}$ to 10^2 seconds. The poroelastic properties adopted in this test case are shown in Table 5.

The numerical solutions for this problem are obtained with the primal $\mathbf{u}-p$ (P1P1) and mixed $\mathbf{u}-p-\sigma_v$ (P1P1P1) formulations, as presented in Eqs. (40) and (44), respectively. The stabilization term, as presented in Eq. (37), can assume different forms depending on the selected formulation and on the choices of a_1, a_2 and a_3. For the primal formulation, Eq. (41) is used with $a_1=1$. For the

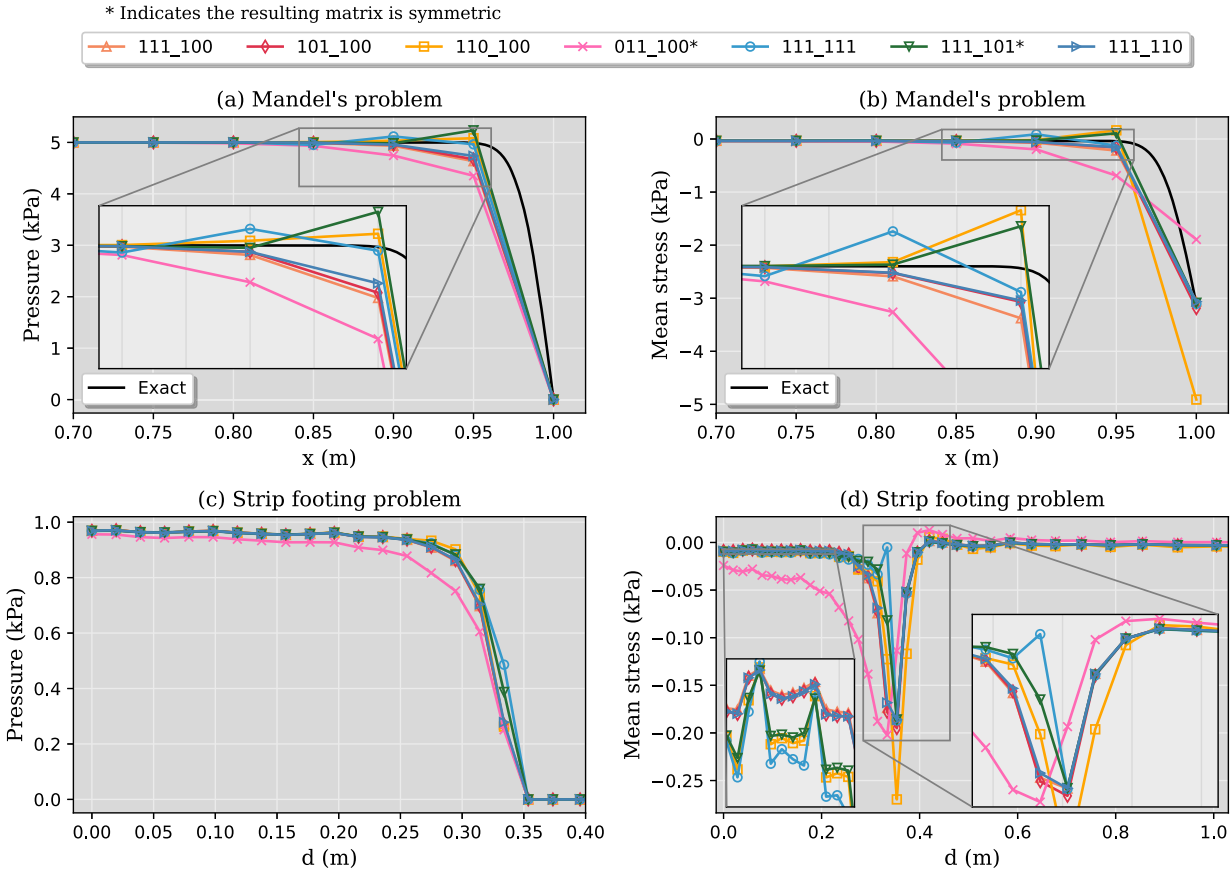

Fig. 12. Numerical results obtained with the mixed poroelastic model considering different stabilization terms into Eq (37) for Eqs. (20) and (21). See Table 4 for clarification on the label terminology.

Table 6
Expressions for the stabilized displacement approximations.

Formulation	Equation	a_1	a_2	a_3	Resulting **u** approximation
Primal	(9)	1	0	0	$\mathbf{u} \approx \mathbf{u}^h - h^2 \frac{\alpha}{G} \nabla p^h$
Mixed	(20)	1	1	1	$\mathbf{u} \approx \mathbf{u}^h - h^2 \frac{\alpha}{G} \nabla p^h + h^2 \frac{3}{E} \nabla \sigma_v^h$
	(21)	1	0	0	$\mathbf{u} \approx \mathbf{u}^h - h^2 \frac{\alpha}{G} \nabla p^h$

mixed formulation, all terms in Eq. (37) are kept when substituted into Eq. (20), while only the pressure term is considered for stabilization of the mass conservation equation (Eq. 21). This is summarized in Table 6.

Fig. 13 shows the analytical solutions for pressure and mean stress profiles compared with the solutions obtained with both primal and mixed formulations. These profiles are shown for the first time step of the simulation $t = 0.0005$ s. It can be observed in Fig. 13 that, as expected, the non-stabilized version (h_0) produce oscillatory pressure and mean stress profiles for both primal and mixed formulations (pressure oscillations are even higher for the mixed formulation). Introducing the stabilization terms into the primal formulation (Fig. 13a and b) significantly smooths out the presence of spurious oscillations in both pressure and mean stress. The results indicate that h_iRad does not dissipate all oscillations, whereas h_Diag is excessively dissipative. Conversely, h_ML appears to be an acceptable compromise, even though small mean stress oscillations are still observed in Fig. 13b. Moving to the mixed formulations (Fig. 13c and d), the same discussion above holds for the pressure profiles, but significant differences are observed for the mean stresses. Fig. 13d confirms the outcome observed with the primal formulation as far as the selection of h is concerned. Another important aspect of these results can be seen in Fig. 13b and d, where the mean stress values can be compared to the exact solution at $x = 1$ m. The primal formulations fall in reproducing correctly the mean stress value at the rightmost boundary, but it is relatively well captured by the mixed formulations, especially with h_ML.

The transient behavior of the numerical solutions for Mandel's problem are shown in Fig. 14. In particular, Fig. 14a and d show a good agreement between exact and numerical solutions for pressure at $x = 0$, with the Mandel-Cryer effect well captured in all cases. A closer look at these figures shows that dissipation added by the stabilization terms slightly shifts the numerical profiles away from

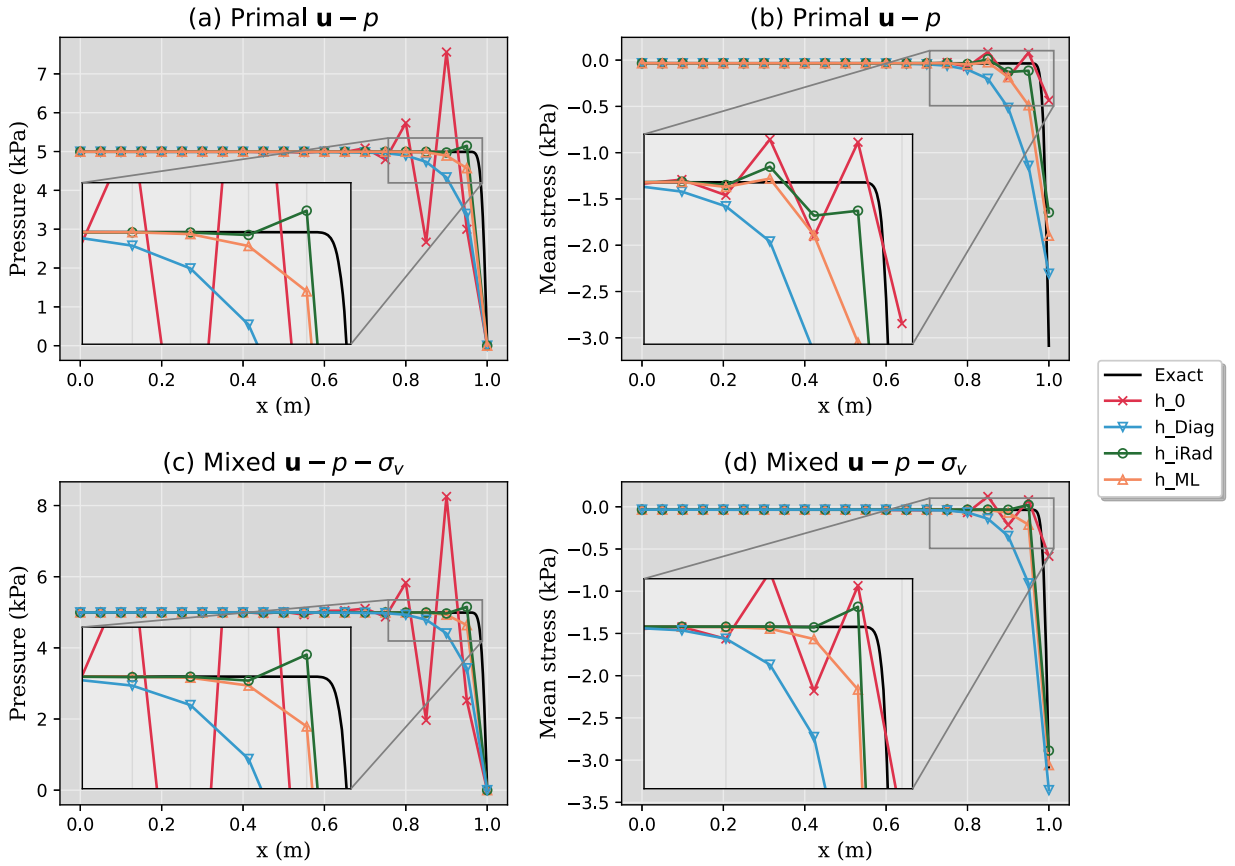

Fig. 13. Mandel's problem: pressure and mean stress profiles obtained with the primal and mixed formulations and compared with the corresponding exact solutions.

the exact solution. This serves as a reminder that stabilization is a compromise between accuracy and physically consistent solutions. The same is valid for the mean stresses at the same position $x = 0$ (Fig. 14b and e). On the other side, Fig. 14c andf reveal that all formulations, especially the primal ones, struggle to capture the mean stress values at the open boundary ($x = 1$ m). Among all the alternatives, the mixed formulation with h_ML is shown to better capture the mean stresses at the open boundary, which is consistent with the results shown in Fig. 13.

9.2.3. Strip footing

The geometry shown in Fig. 6d is considered for the strip footing problem. In this case, a constant load of 100 Pa is applied on the top boundary ($z = 1$ m) in the region between $0 \leq x \leq 0.25$ m and $0 \leq y \leq 0.25$ m. Zero pore pressure is imposed on the top boundary outside the loading region, that is, $x > 0.25$ m and $y > 0.25$ m. All the other boundaries are sealed and prevented from normal displacement. The poroelastic properties and stabilization terms used in this test case are the same as presented in Tables 5 and 6, respectively.

The simulation uses a time discretization of 50 points, logarithmically spaced between $t_1 = 10^{-3}$ s to $t_f = 1.0$ s. According to the results shown in Fig. 15, the mixed formulation without stabilization produces oscillatory patterns for both mean stress and pore pressure. Interestingly, it can be observed that, while the pore pressure oscillations quickly vanish after 0.0012 s, the mean stress oscillations are persistent throughout the entire simulation time. This a natural consequence of the structure of the mass balance equation, which is diffusive and dissipates the pressure perturbation with time. Conversely, the mean stress definition is time-independent, with no mechanism to promote mean stress dissipation. Consequently, mean stress oscillations tend to persist.

To investigate the stabilization scheme, we consider the strip footing problem during undrained response, which occurs in the early instants of the simulation time. The results shown in Fig. 16 refer to the first time step of the simulation (i.e., $t = 0.001$ s). Both primal and mixed formulations present highly oscillatory non-physical pressure patterns, which are successfully removed by adding the stabilization terms. In the stabilized formulations, a careful comparison between the color maps reveals that the pore pressure values on the loading boundary are slightly smaller for the primal formulation compared to the mixed one. This can be better visualized in the right graphs of the same Fig. 16, which shows the pressure profiles on the top boundary along the diagonal $x = y$. These graphs show that the pressure profiles are smoothed out in the stabilized primal formulations compared to their mixed

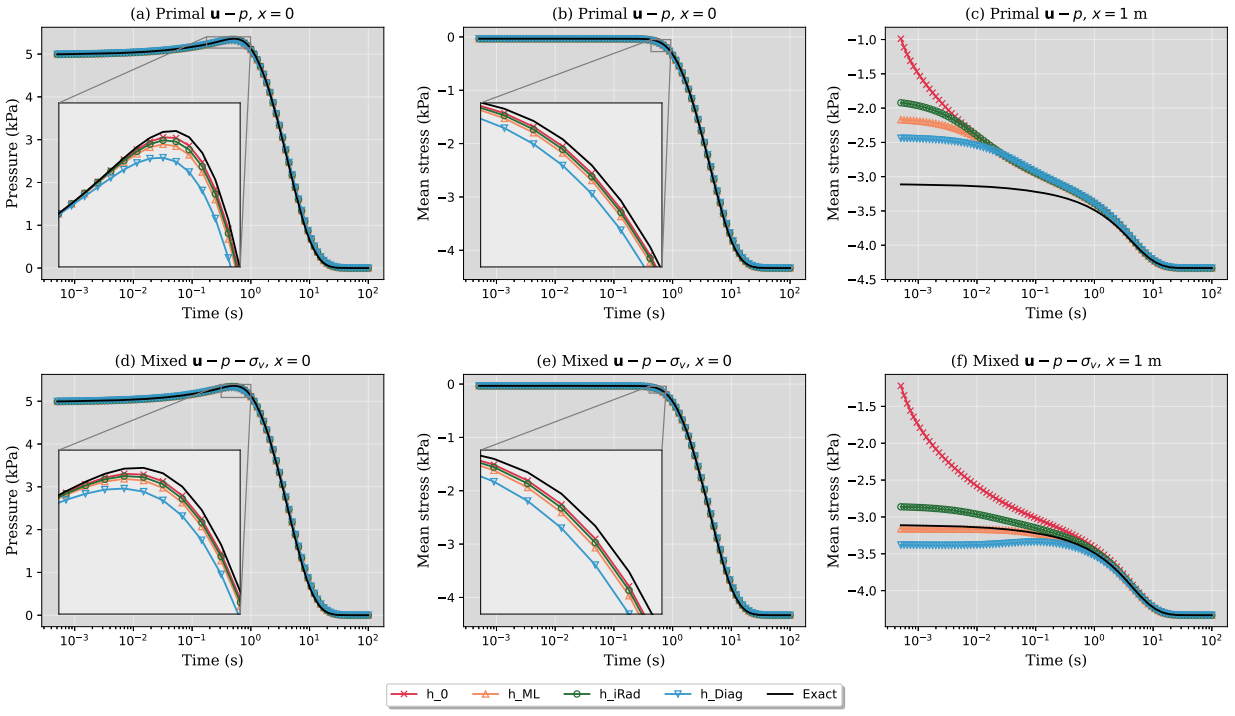

Fig. 14. Mandel's problem: transient behavior of pressure and mean stresses at different positions obtained with both primal and mixed formulations and compared with the exact solutions.

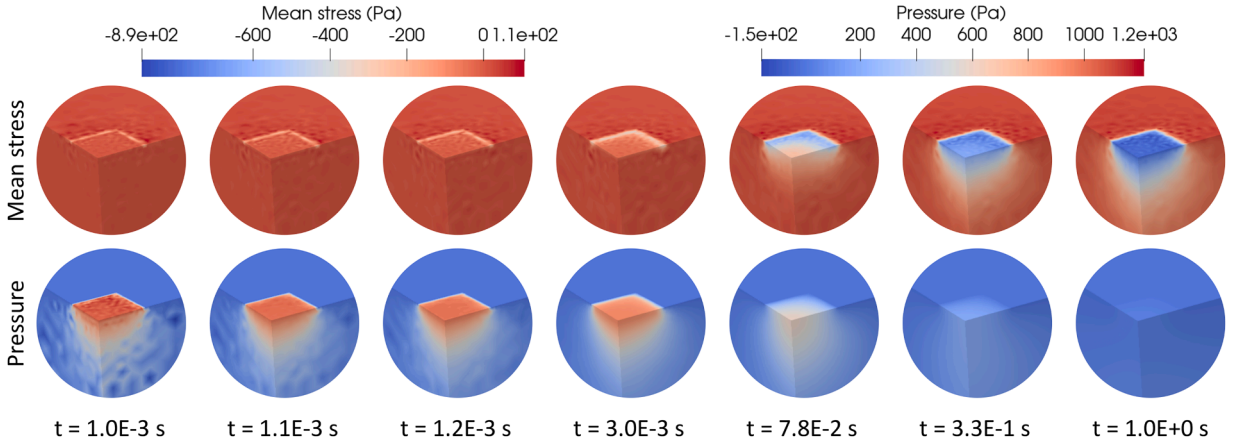

Fig. 15. Mean stress and pore pressure fields for the transient solution of the strip footing problem obtained with the mixed formulation with no stabilization.

counterparts. In other words, the same stabilization strategy introduces more numerical diffusion in the primal formulation than in the mixed one. Moreover, small non-physical oscillations are still apparent in the h_iRad stabilization in both formulations.

While the stabilization strategies satisfactorily eliminate pressure oscillations in both primal and mixed formulations, the same is not observed for the mean stress field. As shown in Fig. 17, the mean stress field for the primal formulations exhibits strong oscillations in all cases. This comes as no surprise, since the primal formulation only allows for pressure stabilization, not mean stress. We emphasize that the Poisson's ratio for this case is 0.3, which is far from the incompressibility limit. This suggests that the observed mean stress oscillations are mainly Gibbs oscillations. Nevertheless, the mean stress stabilization introduced in the mixed formulations are shown to effectively remove spurious oscillations. A careful examination of the mean stress profiles in the bottom-right graph of Fig. 17 shows that (i) h_iRad still present small spurious oscillations, (ii) even smaller oscillations are present in the h_ML results, and (iii) no oscillations are present with h_Diag due to its higher dissipative nature, but accuracy might be compromised for this very same reason.

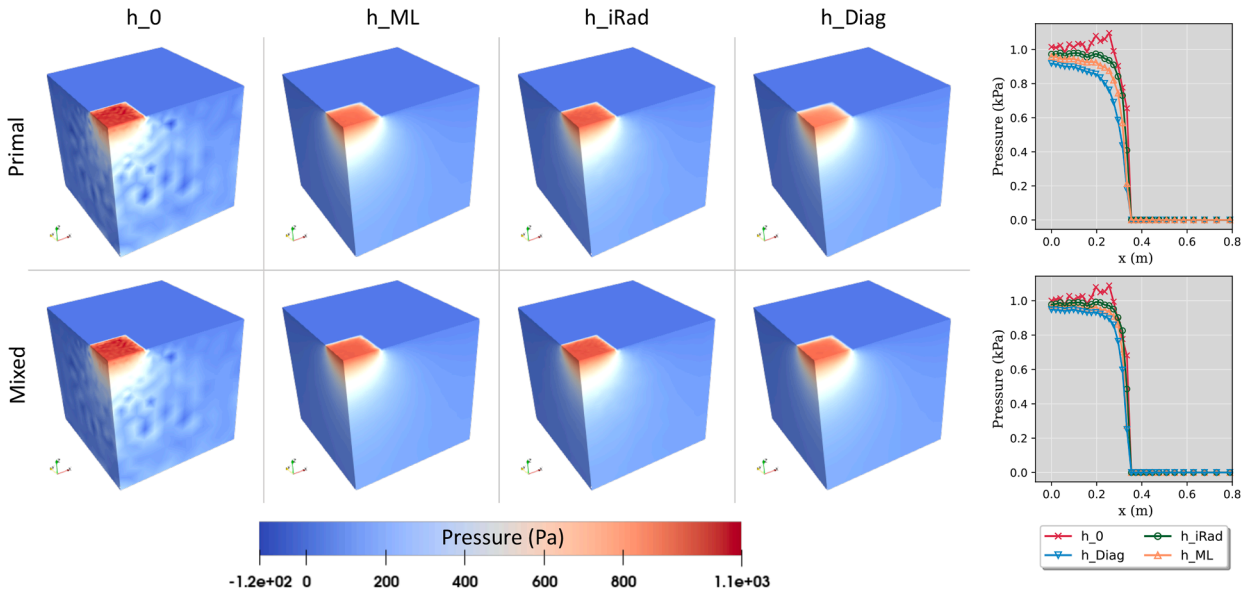

Fig. 16. Strip footing: pressure fields obtained with primal and mixed formulations considering different characteristic lengths for stabilization. (Right) Pressure profiles along the diagonal line at the top boundary ($z = 1$ m and $x = y$).

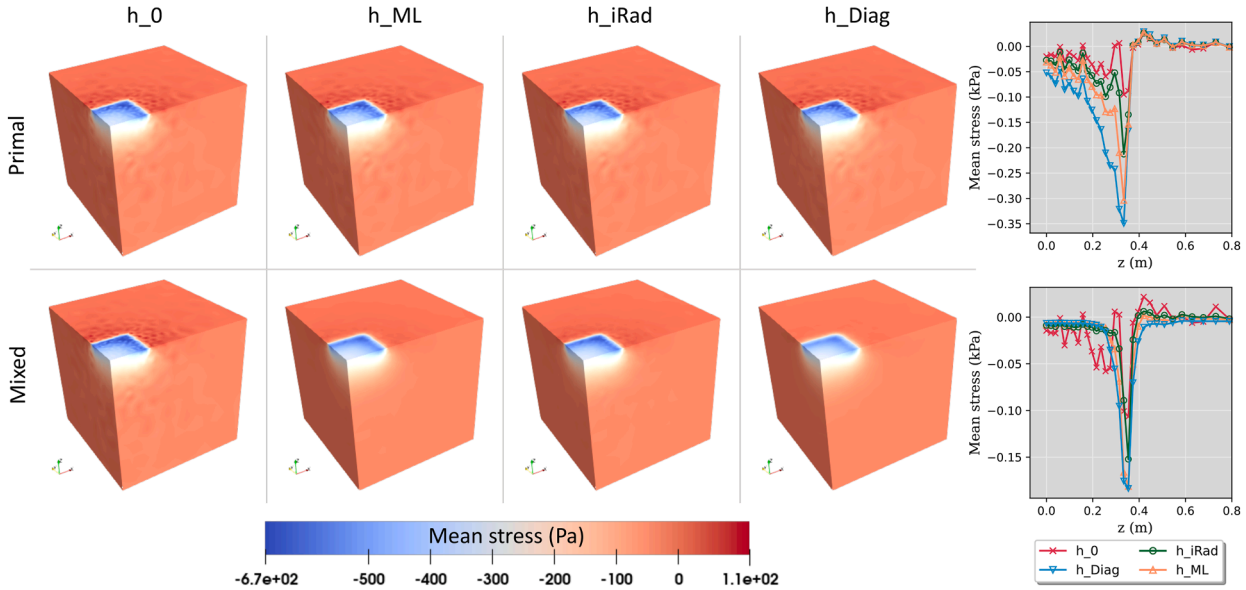

Fig. 17. (Left) Strip footing: mean stress fields obtained with primal and mixed formulations considering different characteristic lengths for stabilization. (Right) Mean stress profiles along the diagonal line at the top boundary ($z = 1$ m and $x = y$).

9.3. Discussion

For the linear elasticity problems, the non-stabilized mixed P1P1 formulation is shown to significantly reduce mean stress oscillations compared to the primal P1 formulation, especially for nearly incompressible solids. However, numerical instabilities can only be eliminated when stabilization terms are added to the weak form. The proposed stabilization strategy, based on the PIS approach, effectively suppresses spurious oscillations across the full range of Poisson's ratio, which includes both saddle-point and Gibbs-type oscillations. Moreover, Fig. 9 shows that P1P1 formulations achieve similar accuracy as the P2P1 formulation at considerably less computational cost. In addition to the test cases, a quantitative stability analysis based on the minimum eigenvalue reveals that the proposed machine learning calculation of the h parameter (h_ML) is the stabilization alternative providing the most robust theoretical outcome. The results obtained from the stability analysis (Fig. 5) are in agreement with Fig. 4b, which shows that h_ML provides the most accurate approximation of the Laplacian of a general polynomial function at the quadrature point. The results presented in the

test cases also confirm the general superiority of the h_ML choice for the h parameter. This is a strong evidence that obtaining a good Laplacian approximation at the quadrature points with appropriate scaling (h) is key to improving stabilization.

The same improvements are also observed for coupled poroelasticity problems. The results obtained for Mandel's problem (Fig. 13) clearly show that (i) h_iRad does not eliminate oscillations, (ii) h_Diag is excessively diffusive, and (iii) h_ML is an effective alternative to eliminate instabilities without compromising accuracy. Moreover, Fig. 14 shows that the primal P1P1 $\mathbf{u}-p$ formulation, irrespective of stabilization, and the non-stabilized mixed P1P1P1 $\mathbf{u}-\sigma_v-p$ formulation are unable to provide accurate calculations of the mean stress field close to the free flow boundary. In contrast, the stabilization terms added to the mean stress equation in the mixed formulation can effectively improve mean stress calculations, with h_ML providing again the most accurate results (see Fig. 14f). It was also shown that, unlike pore pressure, mean stress oscillations do not vanish with time (see Fig. 15), and they can appear even when the material is far from the incompressibility constraint, e.g., $\nu = 0.3$. Finally, the investigation on which term should be included in the stabilization of the mean stress and mass balance equations reveals that this is not a trivial question. For instance, including all stabilization terms in both equations does not produce good results. The combinations that produce symmetric matrices also fail to stabilize the solutions. In general, we suggest to (i) only include the pressure gradient to stabilize the mass balance equation, and (ii) include both the pressure gradient and the full $\left(\frac{3}{E}\nabla\sigma_v\right)$ mean stress terms into the mean stress equation, which was used in this work.

10. Conclusions

This work investigated spurious oscillations in pore pressure and mean stress fields for both linear elasticity and coupled poroelasticity problems using low-order tetrahedral meshes. The investigation focuses on instabilities caused by the Gibbs phenomenon and saddle-point problems. For the linear elasticity model, a single-field ($\mathbf{u}$) primal formulation and a two-field ($\mathbf{u}-\sigma_v$) mixed formulation are considered. Similarly, the usual two-field ($\mathbf{u}-p$) primal formulation for coupled poroelasticity is compared with a proposed three-field ($\mathbf{u}-\sigma_v-p$) mixed formulation. A stabilization scheme is proposed by using Taylor series expansions to obtain an improved approximation for the displacement field $\mathbf{u}$, which requires the computation of (i) parameter h and (ii) the Laplacian of displacement, $\nabla^2\mathbf{u}$. The Physical Influence Scheme (PIS) has been adapted to our finite element formulation to approximate $\nabla^2\mathbf{u}$ based on the underlying physics, which allowed to relate the Laplacian of $\mathbf{u}$ with ∇p and $\nabla\sigma_v$. In addition, we proposed an improved way of computing the parameter h, and proposed a machine learning model to substantially speed up the computations. The combination of PIS with a proper computation of h resulted in a robust stabilization scheme for both p and σ_v, which does not depend on any user-defined tuning parameter. The extension of this stabilization strategy to inelastic deformations is currently under development.

CRediT authorship contribution statement

Hermínio T. Honório: Writing – original draft, Visualization, Validation, Software, Methodology, Formal analysis, Conceptualization; **Andrea Franceschini:** Writing – review & editing, Methodology, Formal analysis, Conceptualization; **Massimiliano Ferronato:** Writing – review & editing, Methodology, Conceptualization; **Hadi Hajibeygi:** Writing – review & editing, Supervision, Methodology, Funding acquisition, Conceptualization.

Data availability

Digital data sets of the results and input data are available upon request.

Declaration of competing interest

Hermínio Tasinafo Honório reports financial support was provided by Energi Simulation. Hermínio Tasinafo Honório reports financial support was provided by Shell Global Solutions International BV. If there are other authors, they declare that they have no known competing financial interests or personal relationships that could have appeared to influence the work reported in this paper.

Acknowledgments

This research was partly supported by Shell Global Solutions International B.V within the project 'SafeInCave', and the Energi Simulation program. The authors also acknowledge members of the ADMIRE and DARSim research groups at TU Delft for the fruitful discussions during the development of this work.

Appendix A. Function approximation

In this section, we develop an expression to approximation a general function ψ at the centroid of an element with cubic shape. Before proceeding with the derivation, let us first define the following notation for conciseness purpose:

$$\psi_p = \psi(\mathbf{x}_p), \tag{A.1}$$

where $\mathbf{x}_p$ represents the spatial coordinates of point p.

Table A.7
Unitary coordinates of the element vertices.

Vertex i	1	2	3	4	5	6	7	8
$\bar{x}_i$	1	−1	−1	1	1	−1	−1	1
$\bar{y}_i$	1	1	−1	−1	1	1	−1	−1
$\bar{z}_i$	−1	−1	−1	−1	1	1	1	1

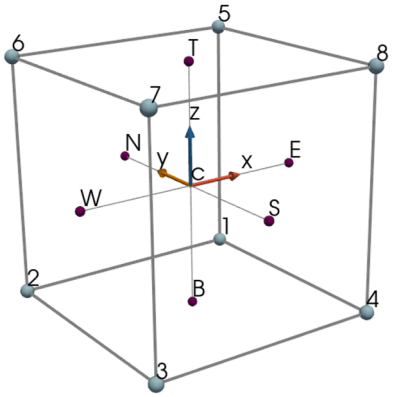

Fig. A.18. Cubic element for Laplacian approximation.

Let us now consider an uniform hexahedral element with edge lengths equal to L, as the one depicted in Fig. A.18. Assume the exact values of a function $\psi(\mathbf{x})$ are known at the element vertices (i.e., $\psi_1, \cdots, \psi_8$) and the Laplacian of ψ is given at the element centroid, that is, $\nabla^2\psi_c$ is known. Based on this data, we show next how to obtain an approximation for a scalar function at the element centroid (i.e., ψ_c) using Taylor series expansions.

The spatial coordinates of each vertex i of the cube illustrated in Fig. A.18 can be represented as

$$\mathbf{x}_i = \frac{L}{2}\begin{bmatrix}\bar{x}_i \\ \bar{y}_i \\ \bar{z}_i\end{bmatrix}, \tag{A.2}$$

where $\bar{x}_i$, $\bar{y}_i$, and $\bar{z}_i$ denote the unitary coordinates of the element vertices, which are summarized in Table A.7.

Using Taylor series to expand from the centroid c to vertex i results in,

$$\psi_i \approx \psi_c + \mathbf{x}_i^T \nabla\psi_c + \frac{1}{2}\mathbf{x}_i^T \mathrm{H}(\psi_c)\mathbf{x}_i, \tag{A.3}$$

where $\mathrm{H}(\psi_c)$ denotes the Hessian matrix of function ψ evaluated at point c, and whose components are given by $H_{ij} = \partial_i\partial_j\psi_c$.

Considering Eq. (A.3) for all element vertices, the values of ψ at each of the faces E, W, N, S, T, and B (see Fig. A.18) are given by,

$$\psi_E \approx \frac{1}{4}(\psi_1 + \psi_4 + \psi_5 + \psi_8) \approx \psi_c + \frac{L}{2}\left.\frac{\partial\psi}{\partial x}\right|_c + \frac{L^2}{8}\nabla^2\psi_c \tag{A.4}$$

$$\psi_W \approx \frac{1}{4}(\psi_2 + \psi_3 + \psi_6 + \psi_7) \approx \psi_c - \frac{L}{2}\left.\frac{\partial\psi}{\partial x}\right|_c + \frac{L^2}{8}\nabla^2\psi_c \tag{A.5}$$

$$\psi_N \approx \frac{1}{4}(\psi_1 + \psi_2 + \psi_5 + \psi_6) \approx \psi_c + \frac{L}{2}\left.\frac{\partial\psi}{\partial y}\right|_c + \frac{L^2}{8}\nabla^2\psi_c \tag{A.6}$$

$$\psi_S \approx \frac{1}{4}(\psi_3 + \psi_4 + \psi_7 + \psi_8) \approx \psi_c - \frac{L}{2}\left.\frac{\partial\psi}{\partial y}\right|_c + \frac{L^2}{8}\nabla^2\psi_c \tag{A.7}$$

$$\psi_T \approx \frac{1}{4}(\psi_5 + \psi_6 + \psi_7 + \psi_8) \approx \psi_c + \frac{L}{2}\left.\frac{\partial\psi}{\partial z}\right|_c + \frac{L^2}{8}\nabla^2\psi_c \tag{A.8}$$

$$\psi_S \approx \frac{1}{4}(\psi_1 + \psi_2 + \psi_3 + \psi_4) \approx \psi_c - \frac{L}{2}\left.\frac{\partial\psi}{\partial z}\right|_c + \frac{L^2}{8}\nabla^2\psi_c \tag{A.9}$$

Finally, adding the above equations all together and solving for ψ_c results in,

$$\psi_c \approx \frac{1}{8}\sum_{i=1}^{8}\psi_i - \frac{L^2}{8}\nabla^2\psi_c. \tag{A.10}$$

Appendix B. Analytical solution for the circular plate hole

From plane strain condition (ε_{zz}), the normal stress in the out-of-plane direction is given by

$$\sigma_{zz} = \nu\left(\sigma_{rr} + \sigma_{\theta\theta}\right),$$

where σ_{rr} and $\sigma_{\theta\theta}$ are the normal stresses in directions r and θ, respectively, cylindrical coordinate system. The mean stress is given by the first stress invariant divided by 3, that is,

$$\sigma_v = \frac{1}{3}\left(\sigma_{rr} + \sigma_{\theta\theta} + \sigma_{zz}\right) = \frac{(1+\nu)}{3}\left(\sigma_{rr} + \sigma_{\theta\theta}\right).$$

The analytical solutions for both σ_{rr} and $\sigma_{\theta\theta}$ are developed in Kirsch [56], producing the following expression for the mean stress field,

$$\sigma_v = \sigma\frac{(1+\nu)}{3}\left[1 - \frac{a^2}{r^2}\left(2 + \frac{a^2}{r^2}\right)\cos 2\theta\right],$$

where σ is the external stress applied to the plate, r is the radius with origin at the center of the circular hole, and θ is measured with respect to the direction of σ.

References

[1] S. Zhang, Battling Gibbs phenomenon: on finite element approximations of discontinuous solutions of PDEs, Comput. Math. Applic. 122 (2022) 35–47. https://doi.org/10.1016/j.camwa.2022.07.014
[2] M.F.P. ten Eikelder, S.K.F. Stoter, Y. Bazilevs, D. Schillinger, Constraints for eliminating the Gibbs phenomenon in finite element approximation spaces, Math. Model. Method. Appl. Sci. 34 (02) (2024) 345–384. https://doi.org/10.1142/S0218202524500040
[3] I. Babuška, Error-bounds for finite element method, Numerische Mathematik 16 (4) (1971) 322–333. https://doi.org/10.1007/BF02165003
[4] F. Brezzi, On the existence, uniqueness and approximation of saddle-point problems arising from Lagrangian multipliers, Publications des séminaires de mathématiques et informatique de Rennes (S4) (1974) 1–26.
[5] F. Brezzi, K.-J. Bathe, A discourse on the stability conditions for mixed finite element formulations, Comput. Method. Appl. Mech. Eng. 82 (1–3) (1990) 27–57. https://doi.org/10.1016/0045-7825(90)90157-H
[6] D.N. Arnold, Mixed finite element methods for elliptic problems, Comput. Method. Appl. Mech. Eng. 82 (1–3) (1990) 281–300. https://doi.org/10.1016/0045-7825(90)90168-L
[7] K.-J. Bathe, Finite Element Procedures, Klaus-Jurgen Bathe, 2006. https://doi.org/10.1002/9780470050118.ecse159
[8] T.J.R. Hughes, The Finite Element Method: Linear Static and Dynamic Finite Element Analysis, Courier Corporation, 2003. https://doi.org/10.1111/j.1467-8667.1989.tb00025.x
[9] T.J.R. Hughes, Equivalence of finite elements for nearly incompressible elasticity, J. Appl. Mech. 44 (1) (1977) 181–183. https://doi.org/10.1115/1.3423994
[10] L.P. Franca, T.J.R. Hughes, A.F.D. Loula, I. Miranda, A new family of stable elements for nearly incompressible elasticity based on a mixed Petrov-Galerkin finite element formulation, Numerische Mathematik 53 (1988) 123–141. https://doi.org/10.1007/BF01395881
[11] T.J.R. Hughes, L.P. Franca, M. Balestra, A new finite element formulation for computational fluid dynamics: V. circumventing the Babuška-Brezzi condition: a stable Petrov-Galerkin formulation of the Stokes problem accommodating equal-order interpolations, Comput. Method. Appl. Mech. Eng. 59 (1) (1986) 85–99. https://doi.org/10.1016/0045-7825(86)90025-3
[12] B. Ramesh, A.M. Maniatty, Stabilized finite element formulation for elastic–plastic finite deformations, Comput. Method. Appl. Mech. Eng. 194 (6–8) (2005) 775–800. https://doi.org/10.1016/j.cma.2004.06.025
[13] O. Klaas, A. Maniatty, M.S. Shephard, A stabilized mixed finite element method for finite elasticity.: formulation for linear displacement and pressure interpolation, Comput. Method. Appl. Mech. Eng. 180 (1–2) (1999) 65–79. https://doi.org/10.1016/S0045-7825(99)00059-6
[14] T.J.R. Hughes, Multiscale phenomena: Green's functions, the Dirichlet-to-Neumann formulation, subgrid scale models, bubbles and the origins of stabilized methods, Comput. Method. Appl. Mech. Eng. 127 (1–4) (1995) 387–401. https://doi.org/10.1016/0045-7825(95)00844-9
[15] T.J.R. Hughes, G.R. Feijóo, L. Mazzei, J.-B. Quincy, The variational multiscale method-a paradigm for computational mechanics, Comput. Method. Appl. Mech. Eng. 166 (1–2) (1998) 3–24. https://doi.org/10.1016/S0045-7825(98)00079-6
[16] A. Masud, K. Xia, A stabilized mixed finite element method for nearly incompressible elasticity, J. Appl. Mech. 72 (72) (2005) 711–720. https://doi.org/10.1115/1.1985433
[17] A. Masud, K. Xia, A variational multiscale method for inelasticity: application to superelasticity in shape memory alloys, Comput. Method. Appl. Mech. Eng. 195 (33–36) (2006) 4512–4531. https://doi.org/10.1016/j.cma.2005.09.014
[18] G. Scovazzi, B. Carnes, X. Zeng, S. Rossi, A simple, stable, and accurate linear tetrahedral finite element for transient, nearly, and fully incompressible solid dynamics: a dynamic variational multiscale approach, Int. J. Numer. Method. Eng. 106 (10) (2016) 799–839. https://doi.org/10.1002/nme.5138
[19] N. Abboud, G. Scovazzi, Elastoplasticity with linear tetrahedral elements: a variational multiscale method, Int. J. Numer. Method. Eng. 115 (8) (2018) 913–955. https://doi.org/10.1002/nme.5831
[20] N. Abboud, G. Scovazzi, A variational multiscale method with linear tetrahedral elements for multiplicative viscoelasticity, Mech. Res. Commun. 112 (2021) 103610. https://doi.org/10.1016/j.mechrescom.2020.103610
[21] K.B. Nakshatrala, A. Masud, K.D. Hjelmstad, On finite element formulations for nearly incompressible linear elasticity, Comput. Mech. 41 (2008) 547–561. https://doi.org/10.1007/s00466-007-0212-8
[22] M. Chiumenti, Q. Valverde, C.A. De Saracibar, M. Cervera, A stabilized formulation for incompressible elasticity using linear displacement and pressure interpolations, Comput. Method. Appl. Mech. Eng. 191 (46) (2002) 5253–5264. https://doi.org/10.1016/S0045-7825(02)00443-7
[23] E. Oñate, Derivation of stabilized equations for numerical solution of advective-diffusive transport and fluid flow problems, Comput. Method. Appl. Mech. Eng. 151 (1–2) (1998) 233–265. https://doi.org/10.1016/S0045-7825(97)00119-9
[24] E. Onate, J. Rojek, R.L. Taylor, O.C. Zienkiewicz, Finite calculus formulation for incompressible solids using linear triangles and tetrahedra, Int. J. Numer. Method. Eng. 59 (11) (2004) 1473–1500. https://doi.org/10.1002/nme.922
[25] F. Brezzi, L.P. Franca, A. Russo, Further considerations on residual-free bubbles for advective-diffusive equations, Comput. Method. Appl. Mech. Eng. 166 (1–2) (1998) 25–33. https://doi.org/10.1016/S0045-7825(98)00080-2
[26] L.P. Franca, A. Russo, Unlocking with residual-free bubbles, Comput. Method. Appl. Mech. Eng. 142 (3–4) (1997) 361–364. https://doi.org/10.1016/S0045-7825(96)01138-3
[27] F. Brezzi, D. Marini, A. Russo, Applications of the pseudo residual-free bubbles to the stabilization of convection-diffusion problems, Comput. Method. Appl. Mech. Eng. 166 (1–2) (1998) 51–63. https://doi.org/10.1016/S0045-7825(98)00082-6
[28] I. Romero, M. Bischoff, Incompatible bubbles: a non-conforming finite element formulation for linear elasticity, Comput. Method. Appl. Mech. Eng. 196 (9–12) (2007) 1662–1672. https://doi.org/10.1016/j.cma.2006.09.010
[29] T.J.R. Hughes, Equivalence of finite elements for nearly incompressible elasticity, J. Appl. Mech. 44 (1) (1977) 181–183. https://doi.org/10.1115/1.3423994

[30] E.A. de Souza Neto, D. Perić, M. Dutko, D. Owen, Design of simple low order finite elements for large strain analysis of nearly incompressible solids, Int. J. Solid. Struct. 33 (20–22) (1996) 3277–3296. https://doi.org/10.1016/0020-7683(95)00259-6
[31] N.E.A. De Souza, F.M.A. Pires, D. Owen, F-Bar-based linear triangles and tetrahedra for finite strain analysis of nearly incompressible solids. part I: formulation and benchmarking, Int. J. Numer. Method. Eng. 62 (3) (2005) 353–383. https://doi.org/10.1002/nme.1187
[32] M.A. Biot, General theory of three-dimensional consolidation, J. Appl. Phys. 12 (2) (1941) 155–164. https://doi.org/10.1063/1.1712886
[33] P.A. Vermeer, A. Verruijt, An accuracy condition for consolidation by finite elements, Int. J. Numer. Anal. Method. Geomech. 5 (1) (1981) 1–14. https://doi.org/10.1002/nag.1610050103
[34] M.A. Murad, A.F.D. Loula, Improved accuracy in finite element analysis of Biot's consolidation problem, Comput. Method. Appl. Mech. Eng. 95 (3) (1992) 359–382. https://doi.org/10.1016/0045-7825(92)90193-N
[35] J. Wan, Stabilized Finite Element Methods for Coupled Geomechanics and Multiphase Flow, Stanford university, 2003.
[36] A. Truty, A Galerkin/least-squares finite element formulation for consolidation, Int. J. Numer. Method. Eng. 52 (8) (2001) 763–786. https://doi.org/10.1002/nme.224
[37] C.R. Dohrmann, P.B. Bochev, A stabilized finite element method for the Stokes problem based on polynomial pressure projections, Int. J. Numer. Method. Fluid. 46 (2) (2004) 183–201. https://doi.org/10.1002/fld.752
[38] J.A. White, R.I. Borja, Stabilized low-order finite elements for coupled solid-deformation/fluid-diffusion and their application to fault zone transients, Comput. Method. Appl. Mech. Eng. 197 (49–50) (2008) 4353–4366. https://doi.org/10.1016/j.cma.2008.05.015
[39] M. Preisig, J.H. Prévost, Stabilization procedures in coupled poromechanics problems: a critical assessment, Int. J. Numer. Anal. Method. Geomech. 35 (11) (2011) 1207–1225. https://doi.org/10.1002/nag.951
[40] A. Truty, T. Zimmermann, Stabilized mixed finite element formulations for materially nonlinear partially saturated two-phase media, Comput. Method. Appl. Mech. Eng. 195 (13–16) (2006) 1517–1546. https://doi.org/10.1016/j.cma.2005.05.044
[41] G.E. Schneider, M.J. Raw, Control volume finite-element method for heat transfer and fluid flow using colocated variables-1. Computational procedure, Numer. Heat Transf., Part A Applic. 11 (4) (1987) 363–390. https://doi.org/10.1080/10407788708913560
[42] M. Darbandi, G. Schneider, K. Javadi, N. Solhpour, The performance of a physical influence scheme in structured triangular grids, in: 41st Aerospace Sciences Meeting and Exhibit, 2003, p. 436. https://doi.org/10.2514/6.2003-436
[43] H. Alisadeghi, S. Karimian, Different modelings of cell-face velocities and their effects on the pressure–velocity coupling, accuracy and convergence of solution, Int. J. Numer. Method. Fluid. 65 (8) (2011) 969–988. https://doi.org/10.1002/fld.2224
[44] S. Vakilipour, M. Mohammadi, V. Badrkhani, S. Ormiston, Developing a physical influence upwind scheme for pressure-based cell-centered finite volume methods, Int. J. Numer. Method. Fluid. 89 (1–2) (2019) 43–70. https://doi.org/10.1002/fld.4682
[45] S. Peters, H.T. Honório, C.R. Maliska, The physical influence scheme applied to staggered unstructured grids for solving fluid flow problems, Numer. Heat Transf., Part B: Fundam. 78 (4) (2020) 197–220. https://doi.org/10.1080/10407790.2020.1787037
[46] H.T. Honório, C.R. Maliska, M. Ferronato, C. Janna, A stabilized element-based finite volume method for poroelastic problems, J. Comput. Phys. 364 (2018) 49–72. https://doi.org/10.1016/j.jcp.2018.03.010
[47] J. Choo, Stabilized mixed continuous/enriched Galerkin formulations for locally mass conservative poromechanics, Comput. Method. Appl. Mech. Eng. 357 (2019) 112568. https://doi.org/10.1016/j.cma.2019.112568
[48] M. Ferronato, M. Frigo, N. Castelletto, J.A. White, Efficient solvers for a stabilized three-field mixed formulation of poroelasticity, in: Numerical Mathematics and Advanced Applications ENUMATH 2019: European Conference, Egmond and Zee, the Netherlands, September 30–October 4, Springer, 2020, pp. 419–427. https://doi.org/10.1007/978-3-030-55874-1_41
[49] M. Frigo, N. Castelletto, M. Ferronato, J.A. White, Efficient solvers for hybridized three-field mixed finite element coupled poromechanics, Comput. Math. Applic. 91 (2021) 36–52. https://doi.org/10.1016/j.camwa.2020.07.010
[50] J.T. Camargo, J.A. White, R.I. Borja, A macroelement stabilization for mixed finite element/finite volume discretizations of multiphase poromechanics, Comput. Geosci. 25 (2021) 775–792. https://doi.org/10.1007/s10596-020-09964-3
[51] J.J. Lee, K.-A. Mardal, R. Winther, Parameter-robust discretization and preconditioning of Biot's consolidation model, SIAM J. Sci. Comput. 39 (1) (2017) A1–A24. https://doi.org/10.1137/15M1029473
[52] K.E. Jansen, S.S. Collis, C. Whiting, F. Shaki, A better consistency for low-order stabilized finite element methods, Comput. Method. Appl. Mech. Eng. 174 (1–2) (1999) 153–170. https://doi.org/10.1016/S0045-7825(98)00284-9
[53] C. Geuzaine, J.-F. Remacle, Gmsh: a 3-D finite element mesh generator with built-in pre-and post-processing facilities, Int. J. Numer. Method. Eng. 79 (11) (2009) 1309–1331. https://doi.org/10.1002/nme.2579
[54] O. Kramer, Scikit-learn, in: Machine Learning for Evolution Strategies, Springer, 2016, pp. 45–53. https://doi.org/10.1007/978-3-319-33383-0
[55] H.C. Elman, D.J. Silvester, A.J. Wathen, Finite Elements And Fast Iterative Solvers: With Applications in Incompressible Fluid Dynamics, Oxford university press, 2014. https://doi.org/10.1093/acprof:oso/9780199678792.001.0001
[56] E.G. Kirsch, Die theorie der elastizit t und die bed rfnisse der festigkeitslehre, Zeitshrift des Vereines deutscher Ingenieure 42 (1898) 797–807.
[57] A. Verruijt, Theory and problems of poroelasticity, Delft Univers. Technol. 71 (2013) 465.